Greedy Growing Enables High-Resolution Pixel-Based Diffusion Models

Anonymous authors
Paper under double-blind review

Abstract

We address the long-standing problem of how to learn effective pixel-based image diffusion models at scale, introducing a remarkably simple greedy method for stable training of large-scale, high-resolution models without the needs for cascaded super-resolution components. The key insight stems from careful pre-training of core components, namely, those responsible for text-to-image alignment *vs.* high resolution rendering. We first demonstrate the benefits of scaling a *Shallow UNet*, with no down(up)-sampling enc(dec)oder. Scaling its deep core layers is shown to improve alignment, object structure, and composition. Building on this core model, we propose a greedy algorithm that grows the architecture into high resolution end-to-end models, while preserving the integrity of the pre-trained representation, stabilizing training, and reducing the need for large high-resolution datasets. This enables a single stage model capable of generating high-resolution images without the need of a super-resolution cascade. Our key results rely on public datasets and show that we are able to train non-cascaded models up to 8B parameters with no further regularization schemes. Vermeer, our full pipeline model trained with internal datasets to produce 1024×1024 images, without cascades, is preferred by 44.0% *vs.* 21.4% human evaluators over SDXL.

1 Introduction

Training large-scale *Pixel-Space text-to-image Diffusion Models* (*PSDM*) to generate high-resolution images has been challenging due to optimization instabilities arising when growing model size and/or target image resolution, and due to the increasing demand for computational resources and high resolution training corpora. The predominant alternatives include *cascaded models*, comprising a sequence of diffusion models each targeting a progressively higher resolution and trained independently (Ho et al., 2022a; Saharia et al., 2022a; Nichol et al., 2022), and *latent diffusion models* (LDMs), where generation is performed in a low-dimensional latent representation, from which high resolution images are generated via a pre-trained latent decoder (Rombach et al., 2022).

In the development of cascaded models, it is challenging to identify sources of quality degradation and distortion resulting from design decisions at specific stages of the model. One well-known issue of cascades is the distribution shift between training and inference, where inputs to super-resolution or decoder models during training are obtained by down-sampling or encoding training images, but during inference they are generated from other models, and hence may deviate from the training distribution. This can cause amplification of unnatural distortions produced by models early in the cascade. The generation of realistic small objects such as faces or hands is one such challenge that has been difficult to diagnose in such models.

Beyond image generation *per se*, diffusion models serve as image priors for myriad downstream tasks, including inverse problems (Jalal et al., 2021; Kadkhodaie & Simoncelli, 2021; Kawar et al., 2022; Song et al., 2023; Chung et al., 2023; Graikos et al., 2022; Tang et al., 2023; Jaini et al., 2023; Zhan et al., 2023; Song et al., 2024), or other generative tasks (Ho et al., 2022b; Levy et al., 2023; Poole et al., 2023; Tan et al., 2023; Bar-Tal et al., 2024; Chen et al., 2023; Tewari et al., 2023). Cascaded diffusion models are not readily applicable to such tasks, and as a consequence, many such applications rely solely on the score function from the base model of a cascade, often at a relatively low resolution. A high resolution end-to-end model would alleviate these issues, but model development and effective training procedures have been elusive.

Figure 1: Images generated with our model Vermeer. (See Appendix A for the prompts.)

Key barriers to training high resolution models include prohibitive resource requirements in both memory and computation. Existent recipes require large batch sizes during training to avoid instabilities, and as a consequence, intractably large amounts of memory for high-resolution images. Another issue concerns the need for high quality, high resolution training data. Existing training methods require large, diverse corpora of text-to-image pairs at the target resolution, while in practice, such data are not readily available at high resolution.

This paper introduces a framework for training high resolution, large-scale text-to-image diffusion models without the use of cascades. To that end we explore the extent to which one can decouple the training of 'visual concepts' associated with textual prompts, from the resolution at which one aims to render the image. Such disentanglement has two goals. It aims at a better understanding of alignment, composition and image fidelity (especially for well-known hard cases like generating consistent hands, text rendering, scene composition, etc.) as a function of model scaling (e.g., see Figure 3). Second, and of equal importance, our framework yields a robust and stable recipe for training large-scale, non-cascaded pixel-based models targeting high-resolution generation. A bonus is that our recipe allows us to jointly train a single model with data comprising multiple resolutions, even if high-resolution text-image pairs are relatively scarce.

The contributions of this paper can be summarized as follows:

- We introduce a novel architecture, Shallow-UViT, which allows one to pretrain the *PSDM*'s core layers on huge datasets of text-image data (subsection 3.2), eliminating the need to train at the

entire model with high resolution images. This also allows us to investigate the emergent properties of PSDM representation scaling in isolation from layers targeting generation at the final resolution.

- We present a *greedy algorithm* for training the Shallow-UViT architecture that allows us to successfully train a high-resolution text-to-image model with small batch sizes (256 versus the typical 2k used in end-to-end solutions) (section 3).

- We show that one can significantly improve different image quality metrics by leveraging the representation pretrained at low-resolution, while growing model resolution in a greedy fashion. Scaling the core components of the Shallow-UViT architecture alone leads to significant improvements in image distribution, quality and text alignment (section 5).

- We demonstrate that these principles work at scale by presenting **Vermeer** (Figure 1), a model trained with our greedy algorithm on large-scale corpora, in conjunction with other well-known methods like asymmetric aspect ratio finetuning, prompt preemption and style tuning (section 6). Vermeer is shown to surpass previous cascaded and auto-regressive models across different metrics. In a human evaluation study with 500 challenging prompts and 25 annotators per image, Vermeer is preferred over SDXL (Podell et al., 2024) by a 2 to 1 margin.

2   Related work

Current high-resolution image generation with diffusion models presents a trade-off between architectural complexity and efficiency. Cascaded diffusion models (Nichol et al., 2022; Dhariwal & Nichol, 2021; Saharia et al., 2022b; Ramesh et al., 2022; Balaji et al., 2022) were originally introduced to circumvent the difficulty of training a single stage, end-to-end model. Cascaded models employ a multi-stage architecture that progressively up-scales lower-resolution images to address the computational challenges of generating high-resolution images directly. Nevertheless, they entail significant complexity and training overhead, as the stages of the cascade are trained independently.

Simple Diffusion (Hoogeboom et al., 2023b) sought to simplify the process by targeting the high resolution generation with a single stage model, introducing a novel UViT architecture and several useful modifications to training methods that improve stability. While this approach is shown to be effective, stability issues remain when targeting large-scale models, and high resolution images, due in part to their dependence on large batch sizes. In this work we adopt a similar UViT architecture, and some of their techniques for scaling, extending the model to much higher resolutions through greedy training. Through scaling the core backbone of the model, and with our greedy training procedure, we find with can scale to much high resolution models ($2\times$ to $8\times$ higher than Simple Diffusion), with excellent alignment, and much smaller batches when training high resolution layers of the model.

Another line of work proposed Matryoshka Diffusion Models (MDM) (Gu et al., 2023) that denoises multiple resolutions using a proposed Nested UNet architecture. They progressively train the network to preserve the representation at higher resolutions. We show in this work an alternate and simpler approach where denoising multiple resolutions is not required, but instead it is crucial to preserve the representation by freezing the pretrained weights as we grow the architecture up to its final design.

On another front, latent diffusion models (LDMs) (Rombach et al., 2022; Jabri et al., 2022; Betker et al., 2023) reduce computational costs by operating within a compressed latent representation. However, LDMs still require separate super-resolution or latent decoder networks to produce final high-resolution images.

The model we introduce also resembles progressive GAN training (Karras et al., 2018) in which layers of increasing resolution are added at each stage. Our work can be thought of as an extension of progressive growing for diffusion models, where we evaluate different growing configurations, and come up with a two-step recipe that arrives at a good trade-off of training efficiency, robustness, and generation quality. Specifically, while all layers remain trainable in progressive GANs, and a sequence of growing operations is performed before reaching the final architecture, we pretrain a core representation that remains frozen when training

all grown layers at once up to the target resolution. We find that this is crucial to preserve the quality of the representation learned at lower resolutions.

3 Method

Our goal is to create a straightforward, stable methodology for training large scale pixel-space diffusion models that operate as a single stage model, i.e., non-cascaded, at inference time. To this end, we first revisit the UNet architecture, aiming to decouple layers that have a major impact on text-to-image alignment (*core components*) from those responsible for rendering at the target image resolution (*encoder-decoder* or *super-resolution components*). Next, we focus on pre-training the core components pretraining and on representation scaling (subsection 3.2). Finally, we present a greedy algorithm to grow the initial architecture core by adding encoder-decoder layers while protecting core layers' representation. This yields a single-stage model at inference time (subsection 3.3).

3.1 Text-to-image core components

UNet is the architecture of choice for diffusion models. Two architecture families are common. In one, convolutional networks comprise a stack of convolutional blocks alternated with pooling or downsampling layers in the encoder, and upsampling layers in the decoder. More recently, the UViT family emerged (Hoogeboom et al., 2023a), in which convolutional blocks are used at the higher layers of the encoder and decoder but augmented with transformer layers at the bottom of the UNet. In both architectural families, text conditioning is accomplished via cross-attention layers, also at the bottom, low-resolution layers of the UNet. In doing so, these layers are responsible for conditioning the models' deepest representation on the textual and/or multi-modal inputs. At these low-resolution layers, the text conditioning signal is able to influence the global image composition while the computational cost of attention is kept relatively low.

Our search for a methodology that allows stable training of large models starts by identifying and isolating *core layers* responsible for text-to-image alignment. Our main conjecture is that it is possible to reduce the instability typically observed during training large-scale PSDMs by warming up layers responsible for text-to-image alignment in isolation from layers responsible for target resolution encoding/decoding.

Specifically, we define the *core components* as those that directly interface with text conditioning signals and those that are crucial in the diffusion process. They can be described as:

- *Text encoding layers* combine one or more textual, character, and/or multimodal pretrained representations (such as those from Raffel et al. (2020b); Xue et al. (2022a); Liu et al. (2023); Radford et al. (2021a)), and project them into the embedding space of the UNet. Typically composed of MLP on top of pooling layers.

- *Core representation layers* comprise hidden layers in the main backbone interfacing with cross-attention layers. They include the bottom layers of the UNet architecture whose features are directly combined with the embedded text by the cross attention operation and layers between them.

- *Time encoding layers* map the diffusion time step into the model's embedding space. Typically designed as a sinusoidal positional encoder, followed by a shallow MLP. Despite not participating directly in the cross-attention operation, it is a core component of the diffusion process.

We isolate these core components of a *PSDM* text-to-image model in order to study their effect on the final model's properties. Next, we propose an architecture that enables the pretraining of these layers, and also supports the study of the properties emerging from scaling them.

3.2 Shallow-UViT

To assist the pretraining of the *core components* and, at the same time investigate the emerging properties from their scaling, we isolate the *core components* training and scaling from other confounding factors in the specification of the UNet's encoder-decoder layers. To that end, we simplify the UNet's conventional
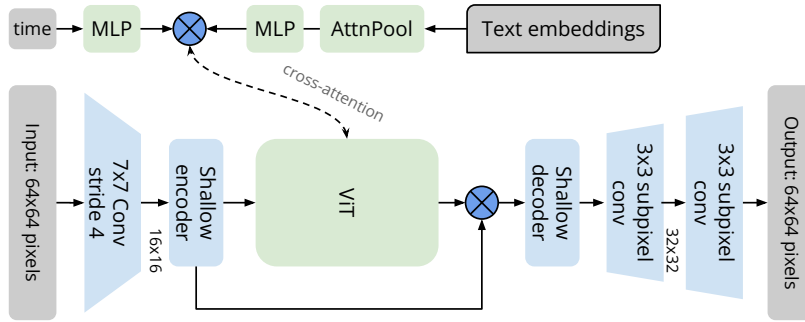
Figure 2: Shallow-UViT architecture: The input image grid is quickly reduced at the entry convolution, while a single residual block with no subsampling layers is used as a shallow encoder and decoder. The layers within the *core components* (in light green) are reused in the final end-to-end architecture, increasing its training stability, while remaining layers are discarded.

hierarchical structure, which operates on multiple resolutions, and define the Shallow-UViT (SU), a simplified architecture comprising a shallow encoder and decoder operating on a fixed spatial grid (Figure 2). Its encoder and decoder have a single residual block each, containing two layers of 3×3 convolutions with swish activations Ramachandran et al. (2017), and no upsampling or downsampling layers. As a result, they share the same spatial grid as the *core representation layers* at the bottom. The first convolutional layer at the entry of the architecture projects the input image into the fixed size grid used by its core layers. A corresponding upsampling head at the model's output reverses this operation. These input/output layers facilitate quickly projecting input images with larger resolution into the core representation with fixed and lower resolution.

As a second simplification, we restrict our investigation to the *core components* from the UViT model family owing to the uniform structure of its *core representation layers*. In contrast, the corresponding layers of convolutional UNets present a broader spectrum of design and hyperparameter choices, owing to their non-uniform yet hierarchical structure, rendering their analysis more complex.

An alternative to the proposed use of the Shallow-UViT architecture, might be to train the *core components* directly as an augmented ViT, as previously explored in latent diffusion models (Peebles & Xie, 2023). Our attempt to explore this approach proved not to be straightforward. A crucial difference between PSDM and LDM becomes highly relevant here. In the case of LDM, the transformer operates on latent tokens, and the diffusion model captures the latent token distribution. Our task, on the other hand, is to pretrain a rich representation directly from the raw pixels, for subsequent reuse as deep features within a higher-resolution pixel-space model. We conjecture that in such approaches the initial layers that are closer to the raw data do not transfer as well when reused within the final model.

Instead, our Shallow-UViT includes proxy additional layers that help with closing the gap between *core components* feature pretraining and their later use. That is, the auxiliary, yet shallow, input (output) and encoding (decoding) layers help adding expressiveness to the transformations between the input (output) and the models' hidden representation. Across the variations explored, the input convolution expands the number input channels up to 256 (we observed no improvement with more channels).

Beyond ablations on scaling (see section 5), we also found that certain variations for the Shallow-UViT composition tend to degrade performance in comparison to our best architecture. In particular, these include the removal of the shallow encoder/decoder blocks; the use of smaller/larger filters ($4 \times 4, 5 \times 5, .., 9 \times 9$) and strides (from 1 up to 8) at the entry convolution; and the use of a single output head with a subpixel convolution upsampling by a factor of 4. We also experimented with convolutional *core representation layers*, but like Dosovitskiy et al. (2021), we find they under-perform their transformed-based counterparts.

3.3 Greedy growing

Here we describe a greedy approach to learn *PSDM*s for high-resolution images. Our process consists of two distinct stages, where we first pretrain the *core representation layers* at a low resolution using a Shallow-UViT architecture. Then, in the second phase, we replace the encoder/decoder layers with a more expressive set of UNet layers and train at the target resolution. This two-stage process is in contrast to progressive growing, which seeks to add one layer at a time. With this approach, we aim to mitigate the well-known instabilities observed during training of large models (Saharia et al., 2022b; Hoogeboom et al., 2023b), while making the best use of the available training corpora.

The *greedy growing* algorithm can be described as follows.

Phase 1   In this phase, the *core components* of the chosen architecture are identified (see subsection 3.1), and a Shallow-UViT model is build on top of them. The Shallow-UViT is trained on the entire training collection of text-image pairs, as it is not limited to high resolution training images.

Phase 2   The second phase greedily grows the Shallow-UViT's encoder/decoder (namely, throwing away the lower-resolution blocks and adding higher-resolution blocks) to obtain the final model. More specifically, this phase adds encoder and decoder layers at different resolutions, while preserving the *core representation layers* at the spatial resolution used during the first phase. In other words, the *core components* continue operating on a 16×16 grid. The added layers are randomly initialized, while the *core components* are initialized with the weights obtained on the first phase. The remaining components of the Shallow-UViT model are discarded.

Next, the grown model is trained. As it is a common practice for the generation of high fidelity images, at this point we filter the training data to remove text-image pairs with either image dimension is lower than the final model's target resolution. The *text encoding layers* and the *core representation layers* are kept frozen, to preserve the richness of the pretrained representation. The *time encoding layers*, on the other hand, are further tuned, jointly with the new encoder and decoder layers introduced in the second phase, which allows it to adapt to changes in the diffusion noise schedule. We adjusted the diffusion logSNR shift for high resolution images as suggested by Hoogeboom et al. (2023b), by a factor of $2 \log(64/d)$. An optional third defrosting phase, may be applied in which all layers are jointly tuned, and seeks to benefit from the full capacity of the end-to-end architecture, but in practice we find that the first two phases are sufficient to obtain a good *PSDM*.

We empirically investigate the behaviour of the proposed algorithm in models of increasing size in subsection 5.2. We investigate the effects of splitting the training of the two tasks in phase one and phase two (i.e., for text-alignment and high-resolution generation), and we compare with models jointly trained from scratch, end-to-end. During these ablations, we constrain the greedy growing phase to use considerably smaller batch sizes than previous work, with no further regularization to demonstrate the optimization stability.

4   Experimental settings

Shallow-UViT: The proposed Shallow-UViT provides a proxy architecture for pre-training the *core components* of a larger PSDM. The ablation studies below us a specific instantiation of the model, but we expect Shallow-UViT to be flexible enough to be used with other component parts. In particular we adopt a combination of two pretrained text encoders for text conditioning: T5-XXL (Raffel et al., 2020a) with 128 sequence length and CLIP (VIT-H14) (Radford et al., 2021b) with 77 sequence length. Given a text prompt, we first tokenize and encode the text using the two encoders independently, and then concatenate the embeddings, yielding a final embedding with sequence length of 205. They are projected into model's *hidden size* by the *text encoding layers*. We keep the Shallow-UViT design fixed, except for changing the capacity by increasing its width (hidden size) and depth (number of transformer's blocks), as detailed in Table 1. That produces a set of models varying from 672M up to 7.7B trainable parameters, mostly dedicated to the *core components*.

---

[1]Number of trainable parameters after ignoring text encoders.

model	transf. blocks	hidden size	MLP channels	heads	params[1]
Shallow-UViT Small	6	1536	6144	12	672M
Shallow-UViT Large	8	2048	8182	16	1.3B
Shallow-UViT Huge	12	3072	12288	24	3.5B
Shallow-UViT XHuge	16	4096	16384	32	7.7B

Table 1: Shallow-UViT variants explored. Transformer layers operating at a 16×16 grid. The components within the shallow encoder and decoder block operate at same spatial resolution and hidden size.

End-to-end model	channels per layer	residual blocks	*params
UViT Small	256-384-768-1536	1-1-1-1	707M
UViT Large	256-512-1024-2048	1-1-1-1	1.4B
UViT Huge	384-768-1536-3072	1-1-1-1	3.6B
UViT XHuge	512-1024-2048-4096	1-1-1-1	7.9B

Table 2: Composition of the encoder-decoder layers grown on top of corresponding Shallow-UViT variants. *core components* identical to the corresponding shallow variant.

We stress that we do not claim that these specific *core components* are optimal. For instance, it is widely recognized that larger pretrained text encoders and longer token sequence lengths increase image quality (Saharia et al., 2022b; Balaji et al., 2022; Podell et al., 2024). Investigating the optimal design of each core component is beyond the scope of this work. Instead, the variations of the Shallow-UViT were intentionally designed to explore the performance benefits gained by increasing *core components*'s capacity independent of the remaining model components.

Greedy growing: In the experiments that follow we consider several different model sizes. Table 1 specifies the Shallow-UViT variants, while Table 2 specifies encoder/decoder parameterizations.

To ablate our hypothesis that greedy growing helps the model learn strong representations with larger, diverse corpora, we also train the full model on a high resolution subset of data used to train the Shallow-UViT; i.e., we simply removed all samples with resolution lower than the target model resolution. To that end, beyond greedy growing, we explore the three training baselines: 1) We create a baseline with all layers trained from scratch on this subset; 2) As an alternative to the frozen phase in the greedy growing, we fine-tune the *core components* on this smaller high resolution subset jointly with the grown components (randomly initialized); and 3) A third baseline adds the optional phase of unfreezing the *core components* after warming up the random weights for 500k steps. Models are trained for 2M steps in total.

The greedy growing algorithm aims to make training large-scale PSDMs at high resolutions more stable. In the case of Simple Diffusion (Hoogeboom et al., 2023b), large batch sizes and regularizers like dropout and multi-scale losses enable end-to-end training from scratch. To stress test the stability and convergence of our greedy growing algorithm, we restrict the batch size to 256 instead of the standard 2k, and we use no other explicit form of regularization. Under that restriction, our largest model (UVit-XHuge) presented numerical instabilities when trained from scratch or fine-tuned, as multiple numerical issues occurred during training. Thus, the results of this large model are presented only for the frozen, and freeze-unfreeze methods. This behaviour confirms observations in previous work and their need for large batch sizes.

Dataset: Rigorous evaluation of generative image models is challenging when models are trained on proprietary datasets. To avoid this issue, we first demonstrate our key findings through extensive empirical evaluations on a publicly available dataset, namely, Conceptual 12M (or CC12M) (Changpinyo et al., 2021).

To evaluate the hypothesis that the greedy algorithm allows one to make good use of available corpora, we trained Shallow-UViT on the entire CC12M training set, while corresponding end-to-end models were trained with CC12M's subset of $8.7M$ images whose dimensions are equal or larger than 512 pixels. Those end-to-end models were therefore trained on 27.5% less data than the corresponding Shallow-UViT model.

We do not explore more aggressive reduction of the corpora as the CC12M dataset is already a relatively small dataset for the models tested, and the variations tested already show overfitting characteristics under this setting, as discussed below. Thus, in what follows, the Shallow-UViT models were trained on 64×64 images, by resizing the smallest dimension of the images to 64 and random cropping along the remaining dimension as needed. The end-to-end models are trained at a target resolution of 512×512 as CC12M does not contain images at resolutions above 1024 pixels.

Full pipeline model: With those findings in place, we then explore the generation of larger images and train on a much larger curated datasets in order to show that the approach scales to state-of-the-art models (section 6). The resulting model, named Vermeer, is used to generate 1024×1024 images, well beyond the scale for which quantitative metrics are readily available. As such, with Vermeer we rely on human evaluation, in comparison to other recent models, like SDXL.

Sampling: Unless mentioned, the images and metrics were produced using 256 steps of a DDPM sampler (Ho et al., 2020) with classifier-free guidance (Ho & Salimans, 2021). We tune the guidance hyper-parameter by a FD-Dino/Clip (VIT-L14) trade-off as described in subsection 5.3.

4.1   Metrics

The evaluation of generative models poses considerable difficulties and constitutes an active research area (Kirstain et al., 2024; Xu et al., 2024; Hessel et al., 2021; Serra et al., 2023; Kim et al., 2024; Lee et al., 2023). In light of its inherent complexity, we utilize a multi-faceted evaluation strategy that combines image distribution metrics, text-alignment metrics and semantic question and answering metrics to validate our intermediary results, but the overall performance of our final model evaluation, Vermeer, is delegated to human evaluators (subsection 6.2). The following criteria are considered:

Image distribution metrics: We evaluate models on three key metrics, namely, the Fréchet Inception Distance (FID) (Heusel et al., 2017), the Fréchet Distance on Dino-v2 feature space (FD-Dino) (Stein et al., 2023; Oquab et al., 2023) and the Clip Maximum Mean Discrepancy (CMMD) distance (Jayasumana et al., 2023). FID is widely used to assess generative image models and select model hyper-parameters, but our findings corroborate its known limitations: it fails to reflect model improvements through training, it does not capture readily apparent distortions in individual images, and it does not correlate well with human perception (Stein et al., 2023; Otani et al., 2023; Jayasumana et al., 2023). Thus, in our study, we do not select training or sampling hyper-parameters solely on the basis of FID but, as described in Appendix 5.3, we review the trade-offs between the observed set of metrics.

We also note that metrics derived from image features vary considerably with image resolution. In what follows we compute metrics using the same resolution as the reference papers. The exception is for CMMD on Shallow-UViT outputs; the original metric taken at 336×336 pixels is dominated by up-sampling effects, obscuring differences between models. Thus, we replaced the original $ViT - L14$ operating at 336×336 by its version at 224×224 pixels.

Multimodal metrics: We adopt CLIP Score as a metric for text-image alignment, as it is widely used, and it complements image distribution metrics above, reflecting the consistency of the generated image with the given prompt. Unlike the original formulation based on ViT-B with path size 32 (Hessel et al., 2021) and previous papers in the area Saharia et al. (2022a); Hoogeboom et al. (2023b), we adopt the ViT-L (patch 14) embedding due to its improved representation. This choice results in lower absolute values of our CLIP Scores compared to previous results, however we noticed that these scores better correlate with the presence of absence of observed distortions.

Semantic QG/A frameworks: One can also automatically generate question-answer pairs with a language model, and then compute image faithfulness by checking whether existing VQA models can answer the questions from the generated image (Hu et al., 2023; Cho et al., 2024). They were intended to address the shortcomings of existing metrics. Despite their effectiveness in evaluating color and material aspects, they often struggle in assessing counting, spatial relationships, and compositions with multiple objects. Such
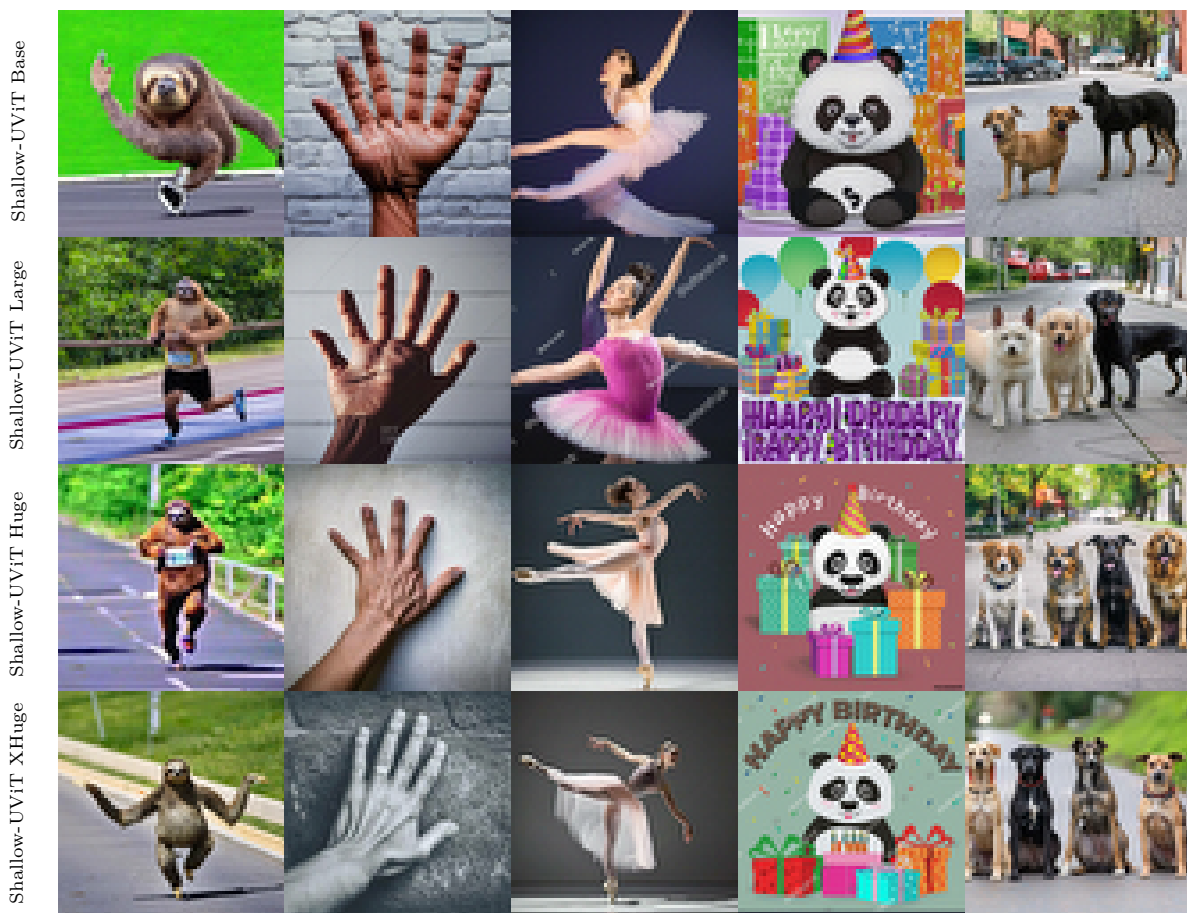
Figure 3: **Qualitative comparison of models with *core components* of increasing size** – Shallow-UViTs trained at 64×64 pixels using CC12M dataset only. Prompts: *'A sloth running a marathon, surprisingly outrunning all competitors.', 'A hand spread out on a wall. DSLR photograph.', 'Close-up portrait of a ballerina in mid-performance, with high motion and dramatic lighting.', 'Word art of "happy birthday", with a smiling panda wearing a party hat, surrounded by gift boxes and a birthday cake.', 'Four dogs on the street.'*

evaluation measures are naturally dependent on the quality of the underlying question generation (QG) and answering (QA) models. Here we adopt DSG (image-text alignment metric) and its set of $1k$ prompts (Cho et al., 2024). The DSG-1k test-prompts cover different challenges (e.g., counting correctly, correct color/shape/text rendering, etc.), semantic categories, and writing styles. A description of the QG, QA used, with qualitative and detailed results, are included in Appendix B.

5 Experiments

5.1 Pretraining and scaling the *core components*

We next use Shallow-UViT as a proxy architecture to investigate the effect of scaling PSDM's *core components*. We train Shallow-UViT variants on 64×64 images from the CC12M dataset for 2k steps. Image distribution metrics and Clip-Score are obtained using $30k$ prompts from the MSCOCO-captions validation set (Chen et al., 2015), while the semantic metrics are extracted on the 1k prompts from DSG-1k (Cho et al., 2024). A summary of the impact of scaling the Shallow-UViT model is given in Tables 3 and 4, while fine grained results on semantic categories are reported in Appendix B. All performance measures indicate

models$_{@64\times64}$	FID$_{30k}\downarrow$	FD-Dino$_{30k}\downarrow$	CMMD$_{30k}\downarrow$	CLIP$_{score}\uparrow$
Shallow-UViT Base	16.97	356.25	0.197	0.234
Shallow-UViT Large	14.80	236.24	0.156	0.240
Shallow-UViT Huge	8.81	133.51	0.139	0.244
Shallow-UViT XHuge	**8.41**	**116.83**	**0.136**	**0.246**

Table 3: Shallow-UViT variants with *core components* of increasing size trained on CC12M at resolution 64×64: Image distribution metrics evaluated on $30k$ samples from MSCOCO captions dataset. Scaling induces performace improvements on image distribution (FID, FD-Dino, CMMD) and text-image alignment ($CLIP_{score}$) metrics simultaneously.

	DSG - VqVa Question Types				
	Entities	Relations	Attributes	Global	DSG($\uparrow$)
#questions:	3378	1485	1722	649	
Shallow-UViT Small	54.38	33.32	43.70	39.98	48.08
Shallow-UViT Large	59.93	39.36	48.75	43.68	52.54
Shallow-UViT Huge	69.18	48.52	54.36	43.30	60.25
Shallow-UViT XHuge	**70.66**	**51.61**	**57.38**	**44.14**	**61.91**

Table 4: Shallow-UVIT evaluated on $1k$ samples from DSG-1k dataset. Scaling *core components* improves performance across all semantic categories. Fine-grained results in Appendix B

significant improvements due to model scaling. A smaller numerical gain is observed in the comparison of the larger two models, but the difference is reflected in qualitative comparisons of the models below.

Figure 3, presents a qualitative comparison of the results the Shallow-UViT variants on challenging prompts. They illustrate the impact of scaling on objects structure, composition and alignment (e.g., with numbers of objects depicted). Despite of the small training dataset, the larger models show significant improvement in generating intricate shapes like hands, body parts and text.

We observed further quantitative improvements across the metrics when training our larger models for longer (Shallow-UViT-Huge and Shallow-UViT-XHuge), but longer training also exhibits overfitting to the CC12 training samples. Figure 4 illustrates images generated using the Shallow-UViT XHuge model with increasing numbers of training steps. As training progresses, the model diverges from the original prompt to produce images that are closer to training samples from the CC12M dataset, and/or representing parts of the prompt only. This hidden phenomena was not associated with changes in the adopted metrics. We conjecture that this effect is largely aggravated by the small size of the training dataset.

Considering the complexity associated with evaluating improvements in representation and the limitations of automatic performance measures, we also ablate the effect of scaling the *core components* under a semantic task that is evaluated by human annotators. In this experiment we consider a *simple counting task*, defined here as the task of generating images of up to 5 objects based on a subset of text prompts from the numerical split of the Gecko benchmark (Wiles et al., 2024). We explore this task as a proxy for gauging both prompt consistency and the model's understanding of objects composition and shapes. It allows less subjective interpretation and noise in human judgments of the model's performance than other image qualities that are influenced by individual preferences. The task of counting under an open set would ultimately imply the ability to keep track of objects. Thus, this ablation emulates a much simpler version of the problem. Figure 5 shows the accuracy improvement associated with scaling observed over 59 prompts. Random condition uses a random number between 1-5. The detailed description of this experiment is presented on Appendix C.

Given the shallow encoder-decoder structure of the Shallow-UViT architecture, we conjecture that the performance improvements observed here, on multiple metrics, are a direct consequence of scaling the *core components*. This hypothesis is further investigated via the reuse of their representation in the next section.

Figure 4: Overfitting and memorization of Shallow-UViT XHuge trained on CC12M. Prompts: (top) *A group of construction workers in the style of 'The Night Watch' by Rembrandt.*; (middle) *A dynamic rendition of a racing cyclist leading their team through a mountain pass, rendered in the style of 'Napoleon Crossing the Alps' by Jacques-Louis David.*; (bottom) *A group of friends enjoying a summer day at a riverside restaurant in the style of 'A Sunday Afternoon on the Island of La Grande Jatte' by Georges Seurat.*
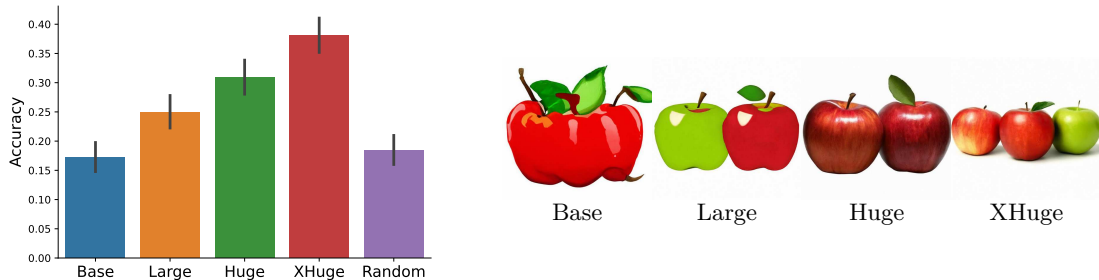
Figure 5: Measuring the impact of scaling on the counting task. Using 59 systematic prompts describing 1-5 objects. Five human annotators reviewed each image (95% bootstrapped confidence intervals are shown). Models with larger *core components* are observed to perform better on counting. Sample prompt: *3 apples.*

model		*tr. params*	*steps*	$\text{FID}_{30k} \downarrow$	$\text{FD-Dino}_{30k} \downarrow$	$\text{CMMD}_{30k} \downarrow$	$\text{CLIP}_{score} \uparrow$
UViT-Base	*scratch*	707M	2M	27.90	624.34	1.355	0.241
	finetuning		2M	23.67	554.99	1.450	0.241
	frozen core	217M	2M	24.68	563.35	1.614	0.235
	freeze-unfreeze	217M/707M	2M	**21.13**	**503.16**	**1.196**	**0.247**
UViT-Large	*scratch*	1.4B	2M	21.73	498.82	1.156	0.247
	finetuning		2M	21.89	414.42	1.160	0.253
	frozen core	351M	2M	**17.68**	**195.80**	**0.752**	**0.264**
	freeze-unfreeze	351M/1.4B	2M	18.37	362.58	0.952	0.256
UViT-Huge	*scratch*	3.6B	2M	18.58	382.17	1.053	0.256
	finetuning		2M	17.52	302.28	0.988	0.264
	frozen core	723M	2M	**15.21**	**156.24**	**0.663**	**0.268**
	freeze-unfreeze	723M/3.6B	2M	16.17	231.94	0.683	0.262
UViT-XHuge	*freeze*	1.2B	2M	**15.32**	**152.12**	**0.571**	**0.269**
	freeze-unfreeze	1.2B/7.9B	2M	16.58	222.38	0.620	0.267

Table 5: End2end variants trained on CC12M dataset at 512×512 pixels and batch size 256: image distribution metrics (FID, FD-Dino and CMMD). Smaller models benefit from finetuning all their parameters. Larger models have more capacity in the encoder-decoder layers, and benefit from freezing the pretrained representations, under such a small batch size regime.

5.2 Experiments on Greedy growing

We next explore greedy growing of Shallow-UViT models to high resolution, non-cascaded models. We compare training models from scratch on the subset of the CC12M dataset filtered by the target resolution (512 pixels) with alternatives for reusing of the *core components* pretrained on the full dataset. They validate our main intuitions behind the greedy growing algorithm, i.e., that the introduction of new, untrained layers, as well as shifts in the distribution of the training data are known causes of the catastrophic forgetting phenomena Vasconcelos et al. (2022); Kuo et al. (2023); Yu et al. (2023) possibly damaging the pre-trained representation.

Tables 5 and 6 summarize performance as a function of model scale for greedy growing, along with various ablations of the training procedure. Our *greedy growing* recipe with frozen *core components*'s and its optional defrosting phase lead to the best results across the metrics. The optional defrosting phase is required for improving the performance of the smallest model ablated (UViT-Base). Its frozen counterpart showed signs of underfitting during training, as it has a small number of trainable parameters (217M) in the added layers. Under this low-capacity scenario, the defrosting phase offers a balance between protecting the *core components* representation and the use of the model's full capacity, as it reduces the degradation of the pretrained representation by warming up the growth layers. Other than this special case, the defrosting phase did not appear to benefit larger models. These quantitative results agree with our hypothesis that the final model benefits from protecting the pretrained representation in our *greedy growing* algorithm.

Figure 6 qualitatively compares generations obtained by finetuning and freezing the *core components*. Additional qualitative comparisons are shown in Appendix D. They illustrate the the benefits of protecting the *core components* from the noise introduced when back-propagating through the randomly initialized growth layers. We observe that the low-resolution images produced by the use of the same representation under their original Shallow-UViT models produce objects whose shapes and parts are correctly defined.

The high-resolution images generated from early steps (20k) of finetuning the *core components* under the UVit architecture present objects with correct shapes superimposed with the diffusion noise. Soon after that (around 50k-100k steps) the quality of object shapes and structure decays as the training backpropagates the noise introduced by the growth layers through the pretrained representation.

Under the *greedy growing* regime and same number of training steps (20k steps) the frozen model is able to produce objects with correct shapes and parts, and maintain their composition as training progresses. Another direct side effect of maintaining the *core components* representation is the fast reduction of the diffusion noise early in training.

model		*steps*	Entities	Relations	Attributes	Global	DSG
				DSG - VqVa Question Types			
UVIT-Base	*scratch*	*2M*	73.16	53.91	62.31	55.55	64.83
	finetuning	*2M*	70.23	49.90	58.89	53.24	62.75
	frozen	*2M*	69.57	49.36	58.22	53.39	61.16
	freeze-unfreeze	*2M*	**73.40**	**53.54**	**62.83**	**56.86**	**66.13**
UVIT-Large	*scratch*	*2M*	73.31	52.02	62.95	58.01	66.02
	finetuning	*2M*	75.01	54.11	65.82	57.86	67.39
	frozen	*2M*	**78.97**	**61.55**	**67.19**	**61.40**	**72.13**
	freeze-unfreeze	*2M*	74.67	55.45	64.08	58.78	67.79
UViT-Huge	*scratch*	*2M*	74.33	55.02	62.98	58.63	66.90
	finetuning	*2M*	77.29	56.40	67.13	62.56	69.67
	frozen	*2M*	**82.59**	**64.65**	**70.35**	**61.86**	**75.15**
	freeze-unfreeze	*2M*	79.04	58.11	65.97	60.86	71.50
UViT-XHuge	*frozen*	*2M*	**83.70**	**66.77**	**70.01**	**62.94**	**75.70**
	freeze-unfreeze	*2M*	81.14	60.44	69.40	60.25	73.53

Table 6: E2e variants at 512×512 pixels trained on CC12M dataset. Metrics evaluated on $1k$ samples from DSG-1k dataset. *DSG* results are aggregated across semantic categories. Fine-grained results in Appendix B.
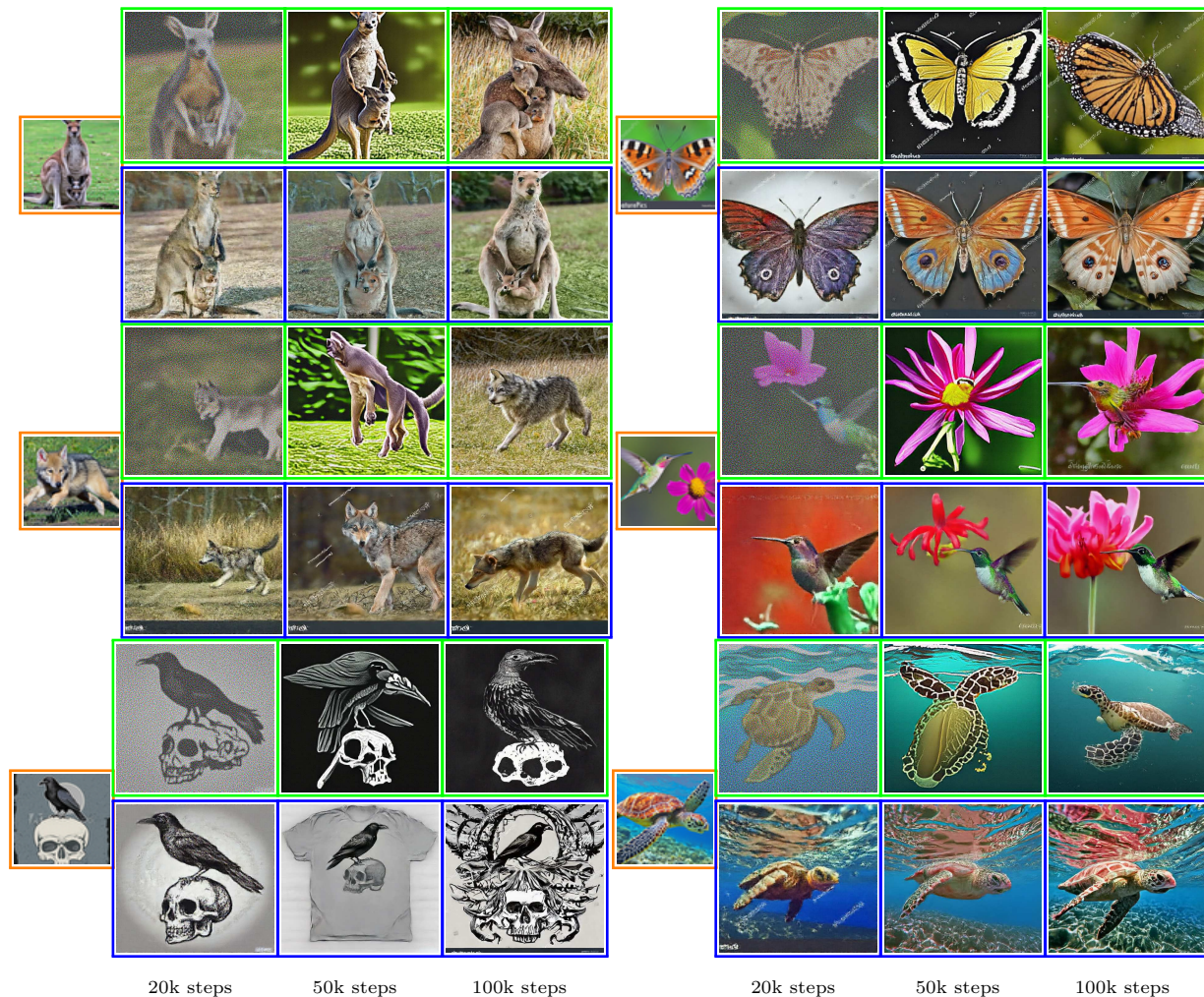
Figure 6: On catastrophic forgetting during early steps of finetuning: the pretrained representation quickly deteriorates due to noise introduced by the random weights from newly added layers. (from left to right) 64×64 image produced by the pretrained Shallow-Unet-Huge; followed by 512×512 images (in green) produced at early steps of finetuning (ft.) the core representation in an E2e model; and (in blue) freezing the core layers. *Differences better observed zooming in.* Prompts: *'A loving mother kangaroo carrying her joey in her pouch.'*; *'A close-up portrait of a butterfly, revealing the intricate patterns and textures on its wings in exquisite detail'*; *'A playful wolf pup chasing its own tail'*; *'A graceful hummingbird hovering near a bright pink flower'*; *'A dark and gothic illustration of a raven perched on a skull'*; *'A determined sea turtle swimming against the ocean current'.*

5.3 Guidance tuning

Diffusion model hyper-parameters affect both training and sampling quality. It is a common practice to tune the sampler guidance weights using FID-CLIP$_{score}$ trade-off curves (Saharia et al., 2022a; Hoogeboom et al., 2023b; Podell et al., 2024). In doing so one aims to strike a balance between images quality (by minimizing FID) and alignment with the text prompt (maximizing the CLIP$_{score}$ score). That said, it is well known that FID does not correlate particularly well with human perception (Stein et al., 2023; Otani et al., 2023; Jayasumana et al., 2023), and large guidance weights are known to increase CLIP-Score but tend to produce over-sharpened, high-contrast images and unrealistic objects (Ho & Salimans, 2021; Saharia et al., 2022b). Due to such limitations, despite widespread use of FID-CLIP$_{score}$ scores for performance comparisons, in practice they are adopted as loose measure of performance, and guidance weights are typically set through qualitative inspection.
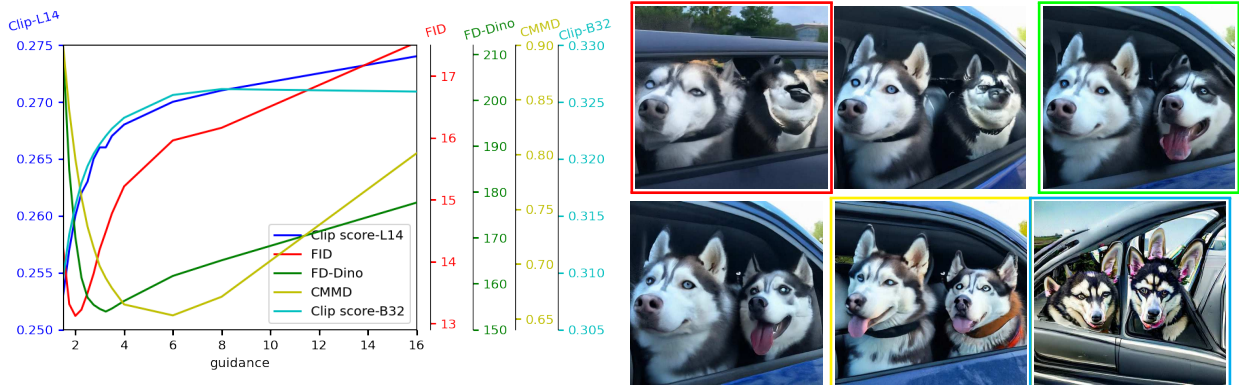
Figure 7: On the FID-CLIP tradeoff and the use of SOTA feature spaces for image and text-alignment distributions. (left) In the process of optimizing guidance, there are clear tradeoffs between different metrics (Fréchet distance and Maximum Mean Discrepancy) taken under different feature spaces (Inception, Dino, and Clip) used to represent the image distributions. (right) qualitative illustrations: sample images taken with increasing guidance values from left-to-right and top-to-bottom. A sample taken under the guidance value that minimizes FID is highlighted with a red bounding box, whereas those using guidance optimum values for minimizing FD-Dino and CMMD are distinguished with green and yellow highlights, respectively. In cyan: the saturation/cartoonish effect of increasing CLIP score further in detriment of the other metrics. *Differences better observed zooming in.* Prompt (from MSCOCO captions): *'Two huskies hanging out of the car windows.'*

Here we explore alternative metrics for hyper-parameters tuning, aiming to better reflect their deployment use, and ultimately human perception. These include recent measures with alternative feature spaces that exhibit better robustness in classification tasks, and align somewhat better with human judgements of image quality and alignment. More specifically, we investigate the use of FD-Dino and CMMD as alternatives to FID in the calibration of the guidance hyper-parameter. Figure 7 plots the response curve of different metrics as a function of guidance weight. They were measured using our UVIT-XHuge frozen model taken over 30k samples from the MSCOCO-caption validation set. It illustrates that the three image distribution metrics are minimized by very different guidance values. Similar curves are observed on the other models and training modalities, in which the best guidance value for minimizing FID, FD-Dino and CMMD are in increasing order. Figure 8 further illustrates samples obtained at the optimal values for each metric, and also when using the maximum guidance tested (16) for increasing CLIP$_{score}$ even further.

A qualitative analysis shows that by minimizing FID, one favors the generation of natural colors and textures, but under closer inspection, it fails to produce realistic object shapes and parts. We conjecture that this matches prior observations on the existence of texture vs shape bias by image classifiers (Geirhos et al., 2019). Guidance values minimizing Dino-v2 features, on the other hand, appear to produce natural color distributions and objects with natural shapes and composition. We adopt the value at this minimum as our new lower bound. Increasing guidance from that value tends to increase color-contrast and sharpening.

Images produced with guidance weights minimizing CMMD tend to produce images with initial signs of saturated colors and over-sharpening. Given its use of Clip features for image distribution comparison, this agrees with previous observations on CLIP$_{score}$. But unlike CLIP$_{score}$ curves, CMMD curves present an inflection point within the range investigated. We use this inflection point to define a closed range for our search of reasonable guidance weights. That is, the range of guidance weights between FD-Dino and CMMD minimums was observed to strike a balance between producing correct shapes and aesthetically pleasing images characterized by enhanced color contrast and sharp edges.

All results presented in this section have their image generated using guidance weights within the FD-Dino/CMMD trade-off range. The specific value selected was taken at the intersection of the optimal ranges of models under the same comparison. Following this approach, our Shallow-UViT results were obtained with guidance weights fixed at 1.75, and their corresponding UViT models with guidance 4.0.

Figure 8: On the use of different metric spaces for calibrating guidance. First three rows: guidance values taken for minimizing respectively FID, FD-Dino and CMMD. The use of robust features is correlated with better shape and composition of images. Last row illustrates the side-effects of further increasing guidance and CLIP-score. Prompts from MSCOCO caption dataset: *'A bathroom with a sink and shower curtain with a map print.'*; *'A person holds a flip phone displaying the screen.'*; *'A motorcycle is parked on a dirt road in a forest.'*; *'A stainless shiny serrated knife sits in front of a sliced loaf.'*; *'A restroom hanging off the side of a building over a mountain.'*

6 A full diffusion pipeline: Vermeer

Vermeer is an 8B parameter model grown from 256 to 1024 pixel resolution. The UViT architecture is similar to our UViT-Huge model (Table 2), except that its bottom layers operate at a grid of 32x32 and with 32 transformer blocks in total. We found that allocating transformer blocks at 32x scale improves details (like small faces). For Vermeer's text encoding, in addition to T5-XXL (Raffel et al., 2020a) and Clip (Radford et al., 2021b) embeddings previously mentioned, we also include a ByT5 (Xue et al., 2022b) encoder with 256 sequence length, resulting in a final embedding with sequence length of 461.

The baseline version (*Vermeer raw model*) is trained with 2k batch size at 256 resolution for 2M iterations, and grown to 1k resolution and finetuned for an additional 1M steps. As illustrated in Figure 1, it supports 3 aspect ratios, i.e., 1024×1024, 768×1376, and 1376×768 thought aspect ratio bucketing (Anlatan, 2022). Once the *raw model* is trained, we apply the following extra steps to improve the aesthetics of the generated images:

- Style finetuning. We train an image classifier based on images that conform to aesthetic and compositional attributes like those described in (Dai et al., 2023), and use it to select 3k images from our

training data as a fine-tuning set. We then fine-tune for 8K steps with a mixture of the original data and the aesthetic subset. We condition the model on the aesthetic subset by adding a token to the text prompt. We found that finetuning the pixel model with a mixture of pretraining and finetuning data is needed to avoid catastrophic forgetting and to avoid the introduction of additional artifacts.

- Distillation. The vanilla Vermeer model adopts 256-step sampling process, making it computationally expensive for real-world use. We employed the multistep consistency model (MCM) (Heek et al., 2024) to distill style-tuned Vermeer to 16 steps, achieving a substantial 16x speedup while maintaining high visual quality.

6.1 Vermeer results

We ablated four steps of Vermeer's development: (i) its raw model resulting from training on a large dataset; (ii) the result of applying prompt engineering at inference to the same model, adding words to improve aesthetic image quality, but with no further training; (iii) the final model, after style finetuning on a curated subset of 3k aesthetically pleasing images; and finally, (iv) its distilled, fast inference variation. Table 7 reports key performance metrics for all four variants, along with Stable Diffusion XL v1.0 (SDXL) (Podell et al., 2024). One can see that the raw model minimizes image distribution metrics that use state of the art feature space, i.e., FD-Dino and CMMD, while CLIP-score suggests a minor drop compared to SDXL. These metrics also highlight a significant shift away from the distribution of MSCOCO-captions (Chen et al., 2015), after augmenting the prompts (*+prompt engineering*) that is further increased when combined with the finetuning of the model for aesthetics pleasing image(*+style finetuning*).

The MSCOCO-captions dataset comprises reference image-caption pairs covering a diverse set of object categories and scenes. Thus, it offers an interesting distribution for measuring image quality and text alignment due to the complexity and diversity of the compositions. At the same time, its use for visual quality preference assessment is spurious as its images were not curated with human aesthetics preferences. On the contrary, many of the images have relatively poor aesthetic appeal. Thus, aiming to improve image aesthetics and composition, during Vermeer's prompt engineering and style tuning phases we intentionally

model		$\text{FID}_{30k} \downarrow$	$\text{FD-Dino}_{30k} \downarrow$	$\text{CMMD}_{30k} \downarrow$	$\text{CLIP}_{score} \uparrow$
$\text{SDXL}_{v1.0}$		**13.19**	185.57	0.898	**0.279**
Vermeer	*raw model*	16.26	**185.25**	**0.631**	0.270
	+prompt engineering	17.33	216.01	0.867	0.269
	+style tuning	24.51	336.25	1.167	0.262
	distilled	25.97	347.19	0.885	0.261

Table 7: Image distribution metrics evaluated on 30k samples of MS-COCO. The raw Vermeer model minimizes distribution metrics that adopt feature spaces from SOTA models (FD-Dino uses Dino-v2 while CMMD adopts Clip features), while tuning it to produce aesthetically pleasing images intentionally diverges from MSCOCO distribution.

model		DSG↑				DSG
		Entities	Relations	Attributes	Global	
SD2.1		75.44	53.06	69.66	68.49	71.23
Muse		77.65	60.64	75.61	67.18	73.09
Imagen Cascade		79.94	62.73	75.73	69.34	75.93
$\text{SDXL}_{v1.0}$		88.04	73.00	78.48	75.19	81.47
Vermeer	*raw model*	86.92	76.36	76.48	68.49	80.77
	+promp eng	87.94	74.92	76.31	67.41	80.99
	+style tunning	88.04	74.21	77.38	69.57	81.16
	+distillation.	84.71	69.23	72.68	65.49	76.88

Table 8: Vermeer. Broad and fine-grained results

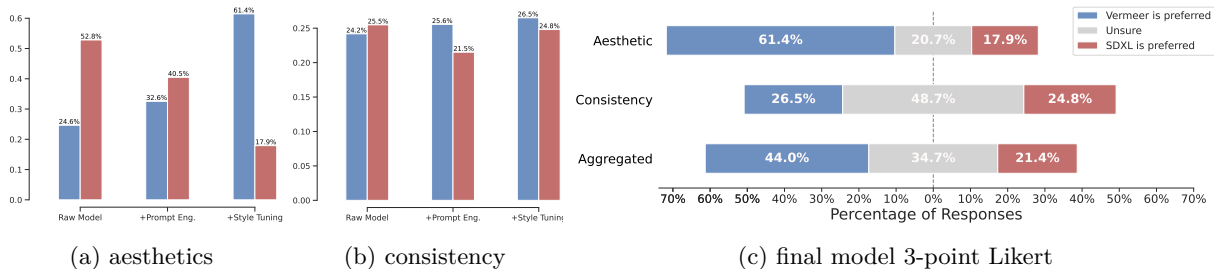(a) aesthetics   (b) consistency   (c) final model 3-point Likert

Figure 9: **Human evaluation results**: Likert plot across 495 prompts, two tasks with 13 users each. Vermeer aesthetic is preferred during 61.4% of all comparisons, while its image-text consistency is marginally preferred. Aggregating the 1k annotations, Veermer is preferred during 44.0% of all comparisons, against 21.0% from SDXL. Prompt engineering and style tuning aligned with human preference for visual aesthetics. Side by side qualitative comparisons in Figure 12 and Figure 13.

move the distribution of images generated by Vermeer away from MSCOCO-caption distribution. To validate this we rely on human evaluation (in the next section).

The effect of the changes on the raw model with the CLIP-score and on semantic metrics on the other hand is minimal, aligned with our observation that the consistency of the model is not much affected by these two procedures. Semantic VqVa results are presented on Table 8. The references to Imagen (Saharia et al., 2022b) and Muse (Chang et al., 2023) models in this table are versions trained on internal data sources thus of similar resources and training pipelines than Vermeer. It shows that Vermeer presents competitive performance with SDXL, and surpassing the other models, including auto-regressive and cascade models.

Finally, we also develop a distilled version of our model, in order to offer an alternative version with faster inference time that similar to the other models presented in this paper operates as a single, non-cascade end-to-end model at inference time. Figure 1 illustrates Vermeer outputs and additional qualitative results including a comparison of samples from the full and distilled versions is presented in Appendix F.

6.2 Human evaluation

Assessing the performance of text-to-image models, ideally, depends on human evaluation, as this complex cognitive process necessitates a profound understanding of text and image relationships. Prior research has demonstrated that many recent works rely exclusively on automated metrics, such as the Fréchet Inception Distance (FID). However, it has been observed that the current automated measures are not fully consistent with human perception in assessing the quality of text-to-image samples (Otani et al., 2023). Thus, to objectively access the quality of images generated by Vermeer, we conduct a side-by-side human evaluation comparing our model with SDXL (Podell et al., 2024).

Setup. In this human evaluation, we ask annotators to evaluate generated images by Vermeer and SDXL based on the same prompt. For this, we collected 495 prompts [2] covering a range of skills: 160 are from TIFA v1.0 targeting measuring the faithfulness of a generated image to its text input covering 12 categories (object, attributes, counting, etc.)(Hu et al., 2023); 200 are sampled from the 1600 Parti Prompts (Yu et al., 2022), selecting for both complexity and diversity of challenges; and 150 others are created fresh for, or are sourced from, more recent prompting strategies targeting challenging cases.

We create two tasks in which we instruct annotators to consider either image quality (aesthetics) or fit to the prompt (consistency), and indicate their preferences using 3-point Liker scale: *Vermeer is preferred, Unsure*, and *SDXL is preferred* (the model names are anonymized). The neural response includes cases that both images are equally good and bad. In the annotation UI, the annotators are shown a prompt along with two images that are randomly shuffled. We collected 13 human ratings per prompt for both aesthetics and consistency (26 ratings per image).

---

[2]We first sampled 510 prompts, and 495 of them were usable after filtering incomplete samples.

Results. Prompt engineering and style tuning are confirmed to have a positive effect on human aesthetics preference (Figure 9, left), and small impact on text consistency (Figure 9, middle). They confirm our conjecture that the decrease on Vermeer's performance based on metrics grounded on the appearance of MSCOCO-caption dataset induced by these two steps are in alignment with the ultimate goal of human preference (Table 7).

Figure 9 (right) plots the Likert scale for our final model in each task (aesthetics or consistency) as well as the aggregated responses (shown in in the bottom bar). Overall, annotators prefer Vermeer 44% of the time, while they select SDXL 21.4% of the time, with relatively fewer *Neutral* responses (34.7%). Vermeer is clearly preferred for its aesthetics, with a win rate of 61.4%, while the gap in consistency between the two models is small, with a difference in the win rate of just 1.7%. Krippendorff's α for aesthetics and consistency are 0.27 and 0.41, respectively, indicating moderate agreement among annotators.

7 Conclusion

We propose a novel recipe for training non-cascaded large scale pixel-space text-to-image diffusion models. It benefits from splitting their training in two phases representing different tasks: learning image-text condition alignment and learning to generate images at high-resolution.

We identified the model *core components* as those responsible for the first task and propose a proxy architecture (Shallow-UViT) to supports its pretraining. The second task is learned with a *greedy growing* algorithm that stacks encoder-decoder layers of the final architecture on top of the pretrained *core components*. When learning the second task, our training recipe preserves the *core components* representation from the noise introduced by the grown layers and their random initialized weights.

Existing non-cascaded models training recipes struggle with scale, if not supported with large batch size and further regularization like dropout and multi-scale loss. Our approach is able to train models up to 8B parameters with small batch size (256) and no further regularization, by pretraining the *core components* and preserving it during the second training phase targeting high-resolution generation.

Compared with training from scratch and finetuning, the greedy growing procedure is more stable, and improves performance on a set of different metrics. Qualitative analysis shows that while keeping the *core components* representation stable it helps to preserve objects shape and overall structure, improving the definition of body parts. Our method allows use of data at different resolutions; the first phase benefits from the larger corpora with minimal requirements on image resolution, while the second phase learn to produce sharp images from the set filtered by the target resolution while reusing the representation learned from the larger set. We also explore models with increasing size, and show the benefits from scaling under different aspects and metrics.

In practice, the non-cascaded solution removes the out-of-distribution shift existent between training and deploying super-resolution phases. Based on that, we present Vermeer, an 8B parameter *Pixel based Text-to-Image Diffusion Model* that produces high-resolution high-quality images using a single non-cascaded model. By training it on a larger dataset, and incorporating a final style tuning phase, Vermeer is able to surpass SDXL v1.0 in human preference study.

References

Anlatan. Novelai improvements on stable diffusion, 2022. URL https://blog.novelai.net/novelai-improvements-on-stable-diffusion-e10d38db82ac.

Yogesh Balaji, Seungjun Nah, Xun Huang, Arash Vahdat, Jiaming Song, Karsten Kreis, Miika Aittala, Timo Aila, Samuli Laine, Bryan Catanzaro, et al. ediffi: Text-to-image diffusion models with an ensemble of expert denoisers. *arXiv preprint arXiv:2211.01324*, 2022.

Omer Bar-Tal, Hila Chefer, Omer Tov, Charles Herrmann, Roni Paiss, Shiran Zada, Ariel Ephrat, Junhwa Hur, Guanghui Liu, Amit Raj, Yuanzhen Li, Michael Rubinstein, Tomer Michaeli, Oliver Wang, Deqing Sun, Tali Dekel, and Inbar Mosseri. Lumiere: A space-time diffusion model for video generation, 2024.

James Betker, Gabriel Goh, Li Jing, Tim Brooks, Jianfeng Wang, Linjie Li, Long Ouyang, Juntang Zhuang, Joyce Lee, Yufei Guo, et al. Improving image generation with better captions. *Computer Science. https://cdn. openai. com/papers/dall-e-3. pdf*, 2(3):8, 2023.

Huiwen Chang, Han Zhang, Jarred Barber, Aaron Maschinot, Jose Lezama, Lu Jiang, Ming-Hsuan Yang, Kevin Patrick Murphy, William T. Freeman, Michael Rubinstein, Yuanzhen Li, and Dilip Krishnan. Muse: Text-to-image generation via masked generative transformers. In Andreas Krause, Emma Brunskill, Kyunghyun Cho, Barbara Engelhardt, Sivan Sabato, and Jonathan Scarlett (eds.), *Proceedings of the 40th International Conference on Machine Learning*, volume 202 of *Proceedings of Machine Learning Research*, pp. 4055–4075. PMLR, 23–29 Jul 2023. URL `https://proceedings.mlr.press/v202/chang23b.html`.

Soravit Changpinyo, Piyush Sharma, Nan Ding, and Radu Soricut. Conceptual 12M: Pushing web-scale image-text pre-training to recognize long-tail visual concepts. In *CVPR*, 2021.

Hansheng Chen, Jiatao Gu, Anpei Chen, Wei Tian, Zhuowen Tu, Lingjie Liu, and Hao Su. Single-stage diffusion nerf: A unified approach to 3d generation and reconstruction. In *ICCV*, 2023. URL `https://arxiv.org/abs/2304.06714`.

Xinlei Chen, Hao Fang, Tsung-Yi Lin, Ramakrishna Vedantam, Saurabh Gupta, Piotr Dollár, and C. Lawrence Zitnick. Microsoft coco captions: Data collection and evaluation server. *CoRR*, abs/1504.00325, 2015. URL `http://dblp.uni-trier.de/db/journals/corr/corr1504.html#ChenFLVGDZ15`.

Jaemin Cho, Yushi Hu, Roopal Garg, Peter Anderson, Ranjay Krishna, Jason Baldridge, Mohit Bansal, Jordi Pont-Tuset, and Su Wang. Davidsonian Scene Graph: Improving Reliability in Fine-Grained Evaluation for Text-to-Image Generation. In *ICLR*, 2024.

Hyungjin Chung, Jeongsol Kim, Michael Thompson Mccann, Marc Louis Klasky, and Jong Chul Ye. Diffusion posterior sampling for general noisy inverse problems. In *The Eleventh International Conference on Learning Representations*, 2023. URL `https://openreview.net/forum?id=OnD9zGAGT0k`.

Xiaoliang Dai, Ji Hou, Chih-Yao Ma, Sam Tsai, Jialiang Wang, Rui Wang, Peizhao Zhang, Simon Vandenhende, Xiaofang Wang, Abhimanyu Dubey, et al. Emu: Enhancing image generation models using photogenic needles in a haystack. *arXiv preprint arXiv:2309.15807*, 2023.

Prafulla Dhariwal and Alexander Nichol. Diffusion models beat gans on image synthesis. *NeurIPS*, pp. 8780–8794, 2021.

Alexey Dosovitskiy, Lucas Beyer, Alexander Kolesnikov, Dirk Weissenborn, Xiaohua Zhai, Thomas Unterthiner, Mostafa Dehghani, Matthias Minderer, Georg Heigold, Sylvain Gelly, Jakob Uszkoreit, and Neil Houlsby. An image is worth 16x16 words: Transformers for image recognition at scale. In *International Conference on Learning Representations*, 2021. URL `https://openreview.net/forum?id=YicbFdNTTy`.

Robert Geirhos, Patricia Rubisch, Claudio Michaelis, Matthias Bethge, Felix A. Wichmann, and Wieland Brendel. Imagenet-trained CNNs are biased towards texture; increasing shape bias improves accuracy and robustness. In *International Conference on Learning Representations*, 2019. URL `https://openreview.net/forum?id=Bygh9j09KX`.

Alexandros Graikos, Nikolay Malkin, Nebojsa Jojic, and Dimitris Samaras. Diffusion models as plug-and-play priors. In Alice H. Oh, Alekh Agarwal, Danielle Belgrave, and Kyunghyun Cho (eds.), *Advances in Neural Information Processing Systems*, 2022. URL `https://openreview.net/forum?id=yhlMZ3iR7Pu`.

Jiatao Gu, Shuangfei Zhai, Yizhe Zhang, Joshua M Susskind, and Navdeep Jaitly. Matryoshka diffusion models. In *The Twelfth International Conference on Learning Representations*, 2023.

Jonathan Heek, Emiel Hoogeboom, and Tim Salimans. Multistep consistency models. 2024.

Jack Hessel, Ari Holtzman, Maxwell Forbes, Ronan Le Bras, and Yejin Choi. Clipscore: A reference-free evaluation metric for image captioning. *arXiv preprint arXiv:2104.08718*, 2021.

Martin Heusel, Hubert Ramsauer, Thomas Unterthiner, Bernhard Nessler, and Sepp Hochreiter. Gans trained by a two time-scale update rule converge to a local nash equilibrium. In *Proceedings of the 31st International Conference on Neural Information Processing Systems*, NIPS'17, pp. 6629–6640, Red Hook, NY, USA, 2017. Curran Associates Inc. ISBN 9781510860964.

Jonathan Ho and Tim Salimans. Classifier-free diffusion guidance. In *NeurIPS 2021 Workshop on Deep Generative Models and Downstream Applications*, 2021. URL https://openreview.net/forum?id=qw8AKxfYbI.

Jonathan Ho, Ajay Jain, and Pieter Abbeel. Denoising diffusion probabilistic models. In H. Larochelle, M. Ranzato, R. Hadsell, M.F. Balcan, and H. Lin (eds.), *Advances in Neural Information Processing Systems*, volume 33, pp. 6840–6851. Curran Associates, Inc., 2020. URL https://proceedings.neurips.cc/paper_files/paper/2020/file/4c5bcfec8584af0d967f1ab10179ca4b-Paper.pdf.

Jonathan Ho, Chitwan Saharia, William Chan, David J. Fleet, Mohammad Norouzi, and Tim Salimans. Cascaded diffusion models for high fidelity image generation. *J. Mach. Learn. Res.*, 23(1), jan 2022a. ISSN 1532-4435.

Jonathan Ho, Tim Salimans, Alexey A. Gritsenko, William Chan, Mohammad Norouzi, and David J. Fleet. Video diffusion models. In *ICLR Workshop on Deep Generative Models for Highly Structured Data*, 2022b. URL https://openreview.net/forum?id=BBelR2NdDZ5.

Emiel Hoogeboom, Jonathan Heek, and Tim Salimans. Simple diffusion: End-to-end diffusion for high resolution images. In *ICML*, 2023a.

Emiel Hoogeboom, Jonathan Heek, and Tim Salimans. Simple diffusion: End-to-end diffusion for high resolution images. In *Proceedings of the 40th International Conference on Machine Learning*, ICML'23. JMLR.org, 2023b.

Yushi Hu, Benlin Liu, Jungo Kasai, Yizhong Wang, Mari Ostendorf, Ranjay Krishna, and Noah A. Smith. Tifa: Accurate and interpretable text-to-image faithfulness evaluation with question answering. In *Proceedings of the IEEE/CVF International Conference on Computer Vision (ICCV)*, pp. 20406–20417, October 2023.

Allan Jabri, David Fleet, and Ting Chen. Scalable adaptive computation for iterative generation. *arXiv preprint arXiv:2212.11972*, 2022.

Priyank Jaini, Kevin Clark, and Robert Geirhos. Intriguing properties of generative classifiers. 2023.

Ajil Jalal, Marius Arvinte, Giannis Daras, Eric Price, Alexandros G Dimakis, and Jon Tamir. Robust compressed sensing mri with deep generative priors. In M. Ranzato, A. Beygelzimer, Y. Dauphin, P.S. Liang, and J. Wortman Vaughan (eds.), *Advances in Neural Information Processing Systems*, volume 34, pp. 14938–14954. Curran Associates, Inc., 2021. URL https://proceedings.neurips.cc/paper_files/paper/2021/file/7d6044e95a16761171b130dcb476a43e-Paper.pdf.

Sadeep Jayasumana, Srikumar Ramalingam, Andreas Veit, Daniel Glasner, Ayan Chakrabarti, and Sanjiv Kumar. Rethinking fid: Towards a better evaluation metric for image generation. *arXiv preprint arXiv:2401.09603*, 2023.

Zahra Kadkhodaie and Eero Simoncelli. Stochastic solutions for linear inverse problems using the prior implicit in a denoiser. In M. Ranzato, A. Beygelzimer, Y. Dauphin, P.S. Liang, and J. Wortman Vaughan (eds.), *Advances in Neural Information Processing Systems*, volume 34, pp. 13242–13254. Curran Associates, Inc., 2021. URL https://proceedings.neurips.cc/paper_files/paper/2021/file/6e28943943dbed3c7f82fc05f269947a-Paper.pdf.

Tero Karras, Timo Aila, Samuli Laine, and Jaakko Lehtinen. Progressive growing of GANs for improved quality, stability, and variation. In *International Conference on Learning Representations*, 2018. URL https://openreview.net/forum?id=Hk99zCeAb.

Bahjat Kawar, Michael Elad, Stefano Ermon, and Jiaming Song. Denoising diffusion restoration models. In Alice H. Oh, Alekh Agarwal, Danielle Belgrave, and Kyunghyun Cho (eds.), *Advances in Neural Information Processing Systems*, 2022. URL https://openreview.net/forum?id=kxXvopt9pWK.

Kyuyoung Kim, Jongheon Jeong, Minyong An, Mohammad Ghavamzadeh, Krishnamurthy Dj Dvijotham, Jinwoo Shin, and Kimin Lee. Confidence-aware reward optimization for fine-tuning text-to-image models. In *The Twelfth International Conference on Learning Representations*, 2024. URL https://openreview.net/forum?id=Let8OMe20n.

Yuval Kirstain, Adam Polyak, Uriel Singer, Shahbuland Matiana, Joe Penna, and Omer Levy. Pick-a-pic: An open dataset of user preferences for text-to-image generation. *Advances in Neural Information Processing Systems*, 36, 2024.

Weicheng Kuo, Yin Cui, Xiuye Gu, AJ Piergiovanni, and Anelia Angelova. Open-vocabulary object detection upon frozen vision and language models. In *The Eleventh International Conference on Learning Representations*, 2023. URL https://openreview.net/forum?id=MIMwy4kh9lf.

Tony Lee, Michihiro Yasunaga, Chenlin Meng, Yifan Mai, Joon Sung Park, Agrim Gupta, Yunzhi Zhang, Deepak Narayanan, Hannah Benita Teufel, Marco Bellagente, Minguk Kang, Taesung Park, Jure Leskovec, Jun-Yan Zhu, Li Fei-Fei, Jiajun Wu, Stefano Ermon, and Percy Liang. Holistic evaluation of text-to-image models. In *Thirty-seventh Conference on Neural Information Processing Systems Datasets and Benchmarks Track*, 2023. URL https://openreview.net/forum?id=qY9LR74O3Z.

Mark Levy, Bruno Di Giorgi, Floris Weers, Angelos Katharopoulos, and Tom Nickson. Controllable music production with diffusion models and guidance gradients. In *NeurIPS*, 2023. URL http://arxiv.org/abs/2311.00613.

Rosanne Liu, Dan Garrette, Chitwan Saharia, William Chan, Adam Roberts, Sharan Narang, Irina Blok, Rj Mical, Mohammad Norouzi, and Noah Constant. Character-aware models improve visual text rendering. In Anna Rogers, Jordan Boyd-Graber, and Naoaki Okazaki (eds.), *Proceedings of the 61st Annual Meeting of the Association for Computational Linguistics (Volume 1: Long Papers)*, pp. 16270–16297, Toronto, Canada, July 2023. Association for Computational Linguistics. doi: 10.18653/v1/2023.acl-long.900. URL https://aclanthology.org/2023.acl-long.900.

Alex Nichol, Prafulla Dhariwal, Aditya Ramesh, Pranav Shyam, Pamela Mishkin, Bob McGrew, Ilya Sutskever, and Mark Chen. GLIDE: Towards photorealistic image generation and editing with text-guided diffusion models. *arXiv preprint arXiv:2112.10741*, 2022.

Andreas Nieder and Stanislas Dehaene. Representation of number in the brain. *Annual review of neuroscience*, 32:185–208, 2009.

Maxime Oquab, Timothée Darcet, Theo Moutakanni, Huy V. Vo, Marc Szafraniec, Vasil Khalidov, Pierre Fernandez, Daniel Haziza, Francisco Massa, Alaaeldin El-Nouby, Russell Howes, Po-Yao Huang, Hu Xu, Vasu Sharma, Shang-Wen Li, Wojciech Galuba, Mike Rabbat, Mido Assran, Nicolas Ballas, Gabriel Synnaeve, Ishan Misra, Herve Jegou, Julien Mairal, Patrick Labatut, Armand Joulin, and Piotr Bojanowski. Dinov2: Learning robust visual features without supervision, 2023.

Mayu Otani, Riku Togashi, Yu Sawai, Ryosuke Ishigami, Yuta Nakashima, Esa Rahtu, Janne Heikkilä, and Shin'ichi Satoh. Toward verifiable and reproducible human evaluation for text-to-image generation. In *Proceedings - 2023 IEEE/CVF Conference on Computer Vision and Pattern Recognition, CVPR 2023*, Proceedings of the IEEE Computer Society Conference on Computer Vision and Pattern Recognition, pp. 14277–14286. IEEE, 2023. doi: 10.1109/CVPR52729.2023.01372. Publisher Copyright: © 2023 IEEE.; IEEE/CVF Conference on Computer Vision and Pattern Recognition ; Conference date: 18-06-2023 Through 22-06-2023.

William Peebles and Saining Xie. Scalable diffusion models with transformers. In *2023 IEEE/CVF International Conference on Computer Vision (ICCV)*, pp. 4172–4182, 2023. doi: 10.1109/ICCV51070.2023.00387.

Dustin Podell, Zion English, Kyle Lacey, Andreas Blattmann, Tim Dockhorn, Jonas Müller, Joe Penna, and Robin Rombach. SDXL: Improving Latent Diffusion Models for High-Resolution Image Synthesis. In *ICLR*, 2024.

Ben Poole, Ajay Jain, Jonathan T. Barron, and Ben Mildenhall. Dreamfusion: Text-to-3d using 2d diffusion. In *The Eleventh International Conference on Learning Representations*, 2023. URL `https://openreview.net/forum?id=FjNys5c7VyY`.

Alec Radford, Jong Wook Kim, Chris Hallacy, Aditya Ramesh, Gabriel Goh, Sandhini Agarwal, Girish Sastry, Amanda Askell, Pamela Mishkin, Jack Clark, Gretchen Krueger, and Ilya Sutskever. Learning transferable visual models from natural language supervision. In Marina Meila and Tong Zhang (eds.), *Proceedings of the 38th International Conference on Machine Learning*, volume 139 of *Proceedings of Machine Learning Research*, pp. 8748–8763. PMLR, 18–24 Jul 2021a. URL `https://proceedings.mlr.press/v139/radford21a.html`.

Alec Radford, Jong Wook Kim, Chris Hallacy, Aditya Ramesh, Gabriel Goh, Sandhini Agarwal, Girish Sastry, Amanda Askell, Pamela Mishkin, Jack Clark, Gretchen Krueger, and Ilya Sutskever. Learning transferable visual models from natural language supervision. In Marina Meila and Tong Zhang (eds.), *Proceedings of the 38th International Conference on Machine Learning*, volume 139 of *Proceedings of Machine Learning Research*, pp. 8748–8763. PMLR, 18–24 Jul 2021b. URL `https://proceedings.mlr.press/v139/radford21a.html`.

Colin Raffel, Noam Shazeer, Adam Roberts, Katherine Lee, Sharan Narang, Michael Matena, Yanqi Zhou, Wei Li, and Peter J. Liu. Exploring the limits of transfer learning with a unified text-to-text transformer. *Journal of Machine Learning Research*, 21(140):1–67, 2020a. URL `http://jmlr.org/papers/v21/20-074.html`.

Colin Raffel, Noam Shazeer, Adam Roberts, Katherine Lee, Sharan Narang, Michael Matena, Yanqi Zhou, Wei Li, and Peter J. Liu. Exploring the limits of transfer learning with a unified text-to-text transformer. *Journal of Machine Learning Research*, 21(140):1–67, 2020b. URL `http://jmlr.org/papers/v21/20-074.html`.

Prajit Ramachandran, Barret Zoph, and Quoc V Le. Searching for activation functions. *arXiv preprint arXiv:1710.05941*, 2017.

Aditya Ramesh, Prafulla Dhariwal, Alex Nichol, Casey Chu, and Mark Chen. Hierarchical text-conditional image generation with clip latents. *arXiv preprint arXiv:2204.06125*, 1(2):3, 2022.

Robin Rombach, Andreas Blattmann, Dominik Lorenz, Patrick Esser, and Björn Ommer. High-resolution image synthesis with latent diffusion models. In *Proceedings of the IEEE/CVF Conference on Computer Vision and Pattern Recognition*, pp. 10684–10695, 2022.

Chitwan Saharia, William Chan, Saurabh Saxena, Lala Li, Jay Whang, Emily Denton, Seyed Kamyar Seyed Ghasemipour, Raphael Gontijo-Lopes, Burcu Karagol Ayan, Tim Salimans, Jonathan Ho, David J. Fleet, and Mohammad Norouzi. Photorealistic text-to-image diffusion models with deep language understanding. In Alice H. Oh, Alekh Agarwal, Danielle Belgrave, and Kyunghyun Cho (eds.), *Advances in Neural Information Processing Systems*, 2022a. URL `https://openreview.net/forum?id=08Yk-n5l2Al`.

Chitwan Saharia, William Chan, Saurabh Saxena, Lala Li, Jay Whang, Emily L Denton, Kamyar Ghasemipour, Raphael Gontijo Lopes, Burcu Karagol Ayan, Tim Salimans, Jonathan Ho, David J Fleet, and Mohammad Norouzi. Photorealistic text-to-image diffusion models with deep language understanding. In S. Koyejo, S. Mohamed, A. Agarwal, D. Belgrave, K. Cho, and A. Oh (eds.), *Advances in Neural Information Processing Systems*, volume 35, pp. 36479–36494. Curran Associates, Inc., 2022b. URL `https://proceedings.neurips.cc/paper_files/paper/2022/file/ec795aeadae0b7d230fa35cbaf04c041-Paper-Conference.pdf`.

Alessio Serra, Fabio Carrara, Maurizio Tesconi, and Fabrizio Falchi. The emotions of the crowd: Learning image sentiment from tweets via cross-modal distillation. *arXiv preprint arXiv:2304.14942*, 2023.

Bowen Song, Soo Min Kwon, Zecheng Zhang, Xinyu Hu, Qing Qu, and Liyue Shen. Solving inverse problems with latent diffusion models via hard data consistency. In *The Twelfth International Conference on Learning Representations*, 2024. URL `https://openreview.net/forum?id=j8hdRqOUhN`.

Jiaming Song, Arash Vahdat, Morteza Mardani, and Jan Kautz. Pseudoinverse-guided diffusion models for inverse problems. In *International Conference on Learning Representations*, 2023. URL `https://openreview.net/forum?id=9_gsMA8MRKQ`.

George Stein, Jesse Cresswell, Rasa Hosseinzadeh, Yi Sui, Brendan Ross, Valentin Villecroze, Zhaoyan Liu, Anthony L Caterini, Eric Taylor, and Gabriel Loaiza-Ganem. Exposing flaws of generative model evaluation metrics and their unfair treatment of diffusion models. In *Advances in Neural Information Processing Systems*, volume 36, 2023.

Vanessa Tan, Junghyun Nam, Juhan Nam, and Junyong Noh. Motion to dance music generation using latent diffusion model. In *SIGGRAPH Asia 2023 Technical Communications*, SA '23, New York, NY, USA, 2023. Association for Computing Machinery. ISBN 9798400703140. doi: 10.1145/3610543.3626164. URL `https://doi.org/10.1145/3610543.3626164`.

Luming Tang, Menglin Jia, Qianqian Wang, Cheng Perng Phoo, and Bharath Hariharan. Emergent correspondence from image diffusion. In *Thirty-seventh Conference on Neural Information Processing Systems*, 2023. URL `https://openreview.net/forum?id=ypOiXjdfnU`.

Ayush Tewari, Tianwei Yin, George Cazenavette, Semon Rezchikov, Joshua B. Tenenbaum, Fredo Durand, William T. Freeman, and Vincent Sitzmann. Diffusion with forward models: Solving stochastic inverse problems without direct supervision. In *Thirty-seventh Conference on Neural Information Processing Systems*, 2023. URL `https://openreview.net/forum?id=gq4xkwQZ1l`.

Cristina Vasconcelos, Vighnesh Nandan Birodkar, and Vincent Dumoulin. Proper reuse of image classification features improves object detection. In *Proceedings of the IEEE/CVF Conference on Computer Vision and Pattern Recognition*, pp. 13628–13637, 2022. URL `https://openaccess.thecvf.com/content/CVPR2022/papers/Vasconcelos_Proper_Reuse_of_Image_Classification_Features_Improves_Object_Detection_CVPR_2022_paper.pdf`.

Olivia Wiles, Chuhan Zhang, Isabela Albuquerque, Ivana Kajic, Su Wang, Emanuele Bugliarello, Yasumasa Onoe, Chris Knutsen, Cyrus Rashtchian, Jordi Pont-Tuset, and Aida Nematzadeh. Revisiting text-to-image evaluation with gecko: On metrics, prompts, and human ratings. *Under review (ECCV)*, 2024.

Jiazheng Xu, Xiao Liu, Yuchen Wu, Yuxuan Tong, Qinkai Li, Ming Ding, Jie Tang, and Yuxiao Dong. Imagereward: Learning and evaluating human preferences for text-to-image generation. *Advances in Neural Information Processing Systems*, 36, 2024.

Linting Xue, Aditya Barua, Noah Constant, Rami Al-Rfou, Sharan Narang, Mihir Kale, Adam Roberts, and Colin Raffel. ByT5: Towards a Token-Free Future with Pre-trained Byte-to-Byte Models. *Transactions of the Association for Computational Linguistics*, 10:291–306, 03 2022a.

Linting Xue, Aditya Barua, Noah Constant, Rami Al-Rfou, Sharan Narang, Mihir Kale, Adam Roberts, and Colin Raffel. Byt5: Towards a token-free future with pre-trained byte-to-byte models. *Transactions of the Association for Computational Linguistics*, 10:291–306, 2022b.

Jiahui Yu, Yuanzhong Xu, Jing Yu Koh, Thang Luong, Gunjan Baid, Zirui Wang, Vijay Vasudevan, Alexander Ku, Yinfei Yang, Burcu Karagol Ayan, Ben Hutchinson, Wei Han, Zarana Parekh, Xin Li, Han Zhang, Jason Baldridge, and Yonghui Wu. Scaling Autoregressive Models for Content-Rich Text-to-Image Generation, 2022.

Qihang Yu, Ju He, Xueqing Deng, Xiaohui Shen, and Liang-Chieh Chen. Convolutions die hard: Open-vocabulary segmentation with single frozen convolutional CLIP. In Alice Oh, Tristan Naumann, Amir Globerson, Kate Saenko, Moritz Hardt, and Sergey Levine (eds.), *Advances in Neural Information Processing Systems 36: Annual Conference on Neural Information Processing Systems 2023, NeurIPS 2023,*

New Orleans, LA, USA, December 10 - 16, 2023, 2023. URL `http://papers.nips.cc/paper_files/paper/2023/hash/661caac7729aa7d8c6b8ac0d39ccbc6a-Abstract-Conference.html`.

Guanqi Zhan, Chuanxia Zheng, Weidi Xie, and Andrew Zisserman. What does stable diffusion know about the 3d scene?, 2023.

A Teaser image prompts

Next, we list the prompts used for generating images at Figure 1 using Vermeer. Their corresponding location is shown in Table 9).

1. the word 'START' written in chalk on a sidewalk
2. a basketball to the left of two soccer balls on a gravel driveway
3. An Egyptian tablet shows an automobile.
4. Macro photography of rose, centered, mini, dark tones, drops of water, cannon
5. photo of a woman's face floating in the water with her eyes closed, you can only see top part of her face above water, reflections, abstract conceptual, realistic reflection, pale sky, scientific photo, high quality fantasy stock photo
6. cyberpunk starship troopers cinematic 4d
7. 3-d Letter "O" made from orange fruit, studio shot, pastel orange background, centered
8. 3-d Letter "W" made from transparent water, studio shot, pastel light blue background, centered
9. 3-d Letter "T" made from tiger fur, studio shot, pastel orange background, centered.
10. Many people carry sacks along a trail through a bright field with long grass and flowers and muted tones. Two small cottages. Dark row of trees. Green hills, blue sky, clouds. Pastoral landscape. Ein plein air. Vibrant, saturation, free brush strokes. Impressionism. Oil on canvas by Auguste Renoir.
11. a photograph of a blue porsche 356 coming around a bend in the road
12. photography of a cat sitting at a sushi restaurant, wearing a blue coat and taking sushi from the boat. Neon bright light, high contrast, low vibrance
13. turtle with German Shepherd dog's head growing from it, DSLR
14. A futuristic street train a rainy street at night in an old European city. Painting by David Friedrich, Claude Monet and John Tenniel.
15. building behind train
16. Realistic photograph of a cute otter zebra mouse in a field at sunset, tall grass, macro 35mm film
17. A 1920's race car with number 7 parked near a fountain in a modern city. Painting by David Friedrich, Claude Monet and John Tenniel.
18. The clock on the bricked building is green. The numbers are in roman numerals. The details have gold accents. The bricked building has a window beside the clock.
19. duck with rabbit's head growing from it, DSLR
20. cauliflower with sheep's head growing from it, DSLR
21. Silver 1963 Ferrari 250 GTO in profile racing along a beach front road. Bokeh, high-quality 4k photograph.
22. a photograph of a knight in shining armor holding a basketball

Table 9: Map of prompts used to generate Vermeer results illustrated in Figure 1

B   Shallow-UViT: Vqva detailed categories

This appendix complements the results on DSG's broad categories presented in the main text by providing their corresponding fine grain results. That is, Table 4 results are complemented with the fine grain detailed results in Table 10, Table 6 with Table 11 and Table 8 with Table 12.

Model		VqVa Question types												
	whole	part	spatial	shape	color	state	type	count	text rendering	texture	global	material	scale	size	DSG
# prompts	2851	517	1477	84	432	740	173	196	116	40	649	92	25	11	
Shallow-UViT Base	0.567	0.412	0.333	0.417	0.550	0.409	0.402	0.523	0.487	0.450	0.400	0.272	0.500	0.318	48.08
Shallow-UViT Large	0.626	0.451	0.395	0.446	0.579	0.478	0.454	0.554	0.552	0.475	0.437	0.353	0.600	0.364	52.54
Shallow-UViT Huge	0.706	0.617	0.488	0.548	0.624	0.530	0.509	0.587	0.552	0.562	0.433	0.424	0.740	0.409	60.25
Shallow-UViT XHuge	0.724	0.617	0.518	0.577	0.646	0.568	0.540	0.582	0.591	0.562	0.441	0.424	0.820	0.636	61.91

Table 10: Shallow-UViT scaling: DSG fine-grained semantic categories. DSG: average score accross DS1K images.

Model		VqVa Question types													
		whole	part	spatial	shape	color	state	type	count	text rendering	texture	global	material	scale	size	DSG
	# prompts	2851	517	1477	84	432	740	173	196	116	40	649	92	25	11	
UVIT-Base	scratch	0.743	0.671	0.540	0.655	0.635	0.639	0.552	0.564	0.690	0.575	0.555	0.489	0.780	0.545	64.83
	finetuning	0.723	0.587	0.500	0.560	0.597	0.596	0.590	0.628	0.625	0.525	0.532	0.478	0.700	0.500	62.75
	frozen	0.702	0.666	0.495	0.560	0.544	0.647	0.566	0.584	0.591	0.613	0.534	0.332	0.640	0.409	61.16
	freeze-unfreeze	0.748	0.657	0.536	0.649	0.650	0.645	0.587	0.640	0.694	0.625	0.569	0.418	0.620	0.455	66.13
UVIT-Large	scratch	0.750	0.642	0.521	0.631	0.642	0.640	0.618	0.643	0.547	0.562	0.580	0.511	0.640	0.591	66.02
	finetuning	0.761	0.688	0.542	0.601	0.681	0.678	0.604	0.666	0.638	0.650	0.579	0.473	0.780	0.636	67.39
	frozen	0.800	0.730	0.616	0.643	0.738	0.684	0.618	0.648	0.728	0.700	0.614	0.418	0.760	0.500	72.13
	freeze-unfreeze	0.761	0.668	0.556	0.571	0.646	0.655	0.665	0.717	0.616	0.625	0.588	0.473	0.840	0.545	67.79
UVIT-Huge	scratch	0.758	0.662	0.551	0.595	0.634	0.645	0.627	0.607	0.698	0.600	0.586	0.505	0.840	0.591	66.90
	finetuning	0.773	0.775	0.565	0.548	0.684	0.716	0.705	0.648	0.659	0.650	0.626	0.484	0.640	0.591	69.67
	frozen	0.827	0.814	0.648	0.649	0.749	0.722	0.685	0.635	0.797	0.688	0.619	0.500	0.820	0.500	75.15
	freeze-unfreeze	0.798	0.748	0.582	0.583	0.675	0.684	0.653	0.666	0.711	0.575	0.609	0.467	0.780	0.500	71.50
UVIT-XHuge	freeze	**0.840**	**0.821**	**0.668**	**0.637**	**0.744**	0.720	**0.720**	**0.671**	**0.668**	**0.688**	0.629	0.473	**0.860**	0.455	**75.70**
	freeze-unfreeze	0.817	0.783	0.607	0.631	0.722	0.705	0.679	0.681	0.681	0.675	0.602	0.533	0.880	0.727	73.53
SD2.1		0.760	0.730	0.530	0.679	0.707	0.729	0.665	0.571	0.655	0.637	0.685	0.495	0.780	0.455	71.23

Table 11: End-to-end models: DSG fine-grained semantic categories. DSG: average score accross DS1K images.

Model		whole	part	spatial	shape	color	state	type	count	text rendering	texture	global	material	scale	size	DSG
							VqVa Question types									
Muse		0.780	0.761	0.605	0.714	0.814	0.766	0.668	0.610	0.651	0.838	0.672	0.647	0.780	0.773	73.09
SD2.1		0.760	0.730	0.530	0.679	0.707	0.729	0.665	0.571	0.655	0.637	0.685	0.495	0.780	0.455	71.23
Imagen Cascade		0.799	0.806	0.626	0.714	0.806	0.772	0.723	0.673	0.750	0.738	0.693	0.641	0.820	0.636	75.93
Imagen Vermeer	raw	0.884	0.787	0.765	0.690	0.810	0.737	0.798	0.689	0.789	0.787	0.685	0.701	0.940	0.773	80.77
	+ prompt eng.	0.892	0.810	0.751	0.750	0.840	0.732	0.809	0.679	0.784	0.825	0.674	0.625	0.880	0.591	80.99
	+ style tuning	0.889	0.833	0.744	0.696	0.836	0.747	0.818	0.714	0.716	0.838	0.696	0.707	0.840	0.591	81.16

Table 12: Vermeer: DSG fine-grained semantic categories .

C   On validating the representation quality improvements from scale by counting

Given the importance of counting and other basic numerical skills in biological intelligence (Nieder & Dehaene, 2009), we expect that competitively performing T2I show similar behaviour when evaluated on such skills. Counting requires manipulation of abstract concepts (numbers) and evaluating this ability provides an objective measure of a well-defined skill. As such it is easier to evaluate and interpret the performance of the model on the counting task, in contrast to some other image characteristics such as aesthetics that might depend on an individual's preferences.

To evaluate models' ability to correctly generate an image with an exact number of objects, we use 59 prompts in the *att/count* category of the Gecko benchmark (Wiles et al., 2024). The Gecko benchmark aims to comprehensively and systematically probe T2I model alignment along different skills such as numerical and spatial reasoning, text rendering, depicting of colors and shapes, and many others.
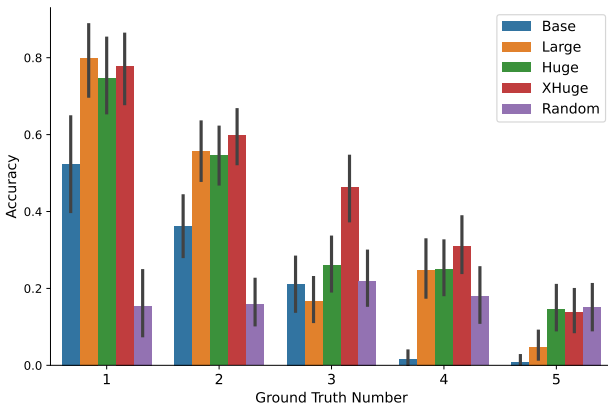
Figure 10: Breakdown of accuracy per number in the original prompt used to generate the image.

Specifically, our analyses include 48 *simple modifier* prompts and 11 *additive* prompts with numbers between 1 and 5. *Simple modifier* prompts are of form "*num noun*" (eg. "1 cat"), where *num* is a number represented by a single digit (ie. 1, 2, 3) or a numeral (ie. "one", "two" or "three") and the noun is a word from a common natural semantic categories such as foods, animals and everyday objects. *Additive* prompts are compositions of individual *simple modifier* prompts as they combine two nouns and two numbers, such as "1 cat and 3 dogs". By using such systematically curated prompts, we are implicitly testing whether models can count, as the ability to correctly generate a number of objects depends on the ability to keep track of objects that were already generated.

To evaluate the correctness of T2I generation of numbers, we recruit human raters through a crowd-sourcing platform to provide the count of objects in every generated image. The study design, including remuneration for the work were reviewed and approved by our institution's independent ethical review committee. We collect 5 annotations per generated image by asking "How many X are there in the image?" where X is the object mentioned in the original prompt used to generate that image. We generate three images for each prompt and each model using different seeds.

Figure 10 shows the breakdown of accuracy per model type as well as per the ground truth number. The ground truth number is the number in the original prompt used to generate the image. The accuracy is the average number of annotations that match the ground truth label for a question and a given model. We observe that all models (with the exception of Base) perform comparably well on generating images with only one object, but this deteriorates with higher number, and only XHuge is able to correctly generate number 3 above the chance level. While exact number generation appears to improve with scale, it is unclear whether this pattern saturates for higher numbers.

D   Qualitative comparison of finetuning and frozen e2e models

Our qualitative comparison between finetuning and frozen *core components* is based on 50 prompts covering different animal species. They are chosen for covering a diverse set of shapes, textures and structures. Figure 11 present a side by side comparison at 50k training steps using the UVIT-Huge model. Structural elements like legs, wings and trunks are better formed when freezing the pretraing *core components* representation. The images were produced with the following list of prompts.

1. "A majestic lion with a flowing mane, basking in the golden African sunset."
2. "A playful dolphin leaping out of the water, glistening with droplets."
3. "A wise old owl perched on a moonlit branch, gazing with piercing yellow eyes."
4. "A colorful macaw soaring through a lush, vibrant rainforest."
5. "A mischievous raccoon rummaging through a trash can in a suburban backyard."

Figure 11: On the reuse of the core layers: qualitative results. Finetune (green bounding boxes) × Frozen results (blue bounding boxes) at $50k$ steps. Images at $512 \times 512 pixels$. Models trained with CC12M. Freezing the representation induces objects with better global and parts structure, from the very early steps of training.

6. "A close-up portrait of a fluffy panda munching on bamboo."

7. "A graceful hummingbird hovering near a bright pink flower."

8. "A herd of elephants silhouetted against a fiery orange sky."

9. "A group of meerkats standing alert in the desert, looking out for danger."

10. "A photorealistic image of a chameleon blending seamlessly with its surroundings."

11. "A Van Gogh-inspired painting of sunflowers with butterflies flitting around them."

12. "A pixel art rendition of a pixelated cat chasing a pixelated mouse."

13. "A watercolor painting of a majestic tiger stalking through a bamboo forest."

14. "A surreal landscape with a melting elephant in the style of Salvador Dalí."

15. "A vibrant pop art image of a zebra with bold stripes and contrasting colors."

16. "A cubist artwork depicting a fragmented and reassembled bear."

17. "A pointillist painting of a turtle, created with tiny dots of color."
18. "A minimalist line drawing of a graceful swan."
19. "A whimsical cartoon illustration of a group of singing frogs in a pond."
20. "A dark and gothic illustration of a raven perched on a skull."
21. "A penguin riding a surfboard on a giant tropical wave."
22. "A giraffe wearing a top hat and monocle, enjoying a cup of tea in a fancy cafe."
23. "A zebra crossing a busy city street at a crosswalk."
24. "A cat wearing a space suit, exploring the surface of Mars."
25. "A monkey DJ mixing beats at a neon-lit dance club."
26. "An octopus painting a self-portrait with its many arms."
27. "A sloth running a marathon, surprisingly outrunning all competitors."
28. "A polar bear relaxing in a hot tub in the middle of the Arctic."
29. "A group of rabbits building a snowman in a winter wonderland."
30. "A dog astronaut floating in space, gazing at the Earth."
31. "A grumpy bulldog wearing a birthday hat and refusing to smile."
32. "A joyful rabbit hopping through a field of wildflowers."
33. "A curious chimpanzee looking intently through a magnifying glass."
34. "A proud peacock displaying its magnificent tail feathers."
35. "A loving mother kangaroo carrying her joey in her pouch."
36. "A mischievous squirrel hiding nuts in a tree trunk."
37. "A sleepy koala clinging to a tree branch, taking a nap."
38. "A determined sea turtle swimming against the ocean current."
39. "A playful wolf pup chasing its own tail."
40. "A group of penguins waddling together in a comical huddle."
41. "A chameleon painted with the vibrant colors of a bustling city skyline." (Imagine a chameleon camouflaged with neon signs and skyscraper patterns.)
42. "A flock of birds forming the shape of a musical note in flight." (Visualize a dynamic dance of birds creating a melody in the sky.)
43. "A fishbowl on the moon, with an astronaut goldfish gazing at Earth." (A whimsical and thought-provoking perspective shift.)
44. "A microscopic landscape teeming with life, where insects are giants and blades of grass are towering trees."
45. "A cat wearing a crown and royal robe, sitting regally on a throne made of yarn balls." (A playful portrait with a touch of humor.) **
46. "A photorealistic image of extinct animals roaming in a modern city landscape." ** (Blend the past and present for a surreal scene.)
47. "An underwater ballet performed by graceful sea creatures." (Capture the beauty and movement of marine life in an artistic way.)
48. "A hedgehog painted as a starry night sky, with its spines representing twinkling stars." (A dreamy fusion of nature and the cosmos.)
49. "Animals playing musical instruments together in a harmonious orchestra." (Imagine the symphony created by a unique animal band.)
50. "A close-up portrait of a butterfly, revealing the intricate patterns and textures on its wings in exquisite detail." (Appreciate the delicate beauty of nature.)

E Human evaluation

This appendix complements the human evaluation quantitative results presented in subsection 6.2, with some illustrations of the examples compared. Figure 12 and Figure 13 illustrate winning, losing, and matching cases for respectively the visual aesthetic and text consistency tasks. During the ranking, the image order was shuffled, but kept in fixed ordered in these illustrations for readability only. Pairs were selected to illustrate responses observed to reach 'Perfect agreement' (all raters agreed with the winning class), 'Strong agreement' (12-10 of the 13 raters agreed), 'Majority agreement' (9-7 of the 13 raters agreed) and 'Weak agreement' (6-5 of the 13 raters agreed on the winning class). They illustrate the model's and the preference agreement variability across different prompts. Thus, these qualitative examples further sustain our choice for covering a large number and diverse set of prompts on our human evaluation settings. While raters clearly agree when one of the images contains the presence of an artifact (see Figure 12 SDXL's Treehouse and panda bear with multiple glasses) or cases in which the models clearly have not followed the text description (In Figure 13 first row Vermeer image is missing the microphone, while SDXL raccoon lizard shows a regular raccoon), some prompts lead to generations that can be argued as equally good (as in the forest path in Figure 12) or equally bad (as in "two laptops a mouse cords wires and a monitor").

We favored the coverage of a large number of challenging prompts following the observation that the different models' performance vary across different query modes. Overall, evaluating human preferences in generative models remains a complex and unresolved issue. To our knowledge, there is no widely accepted protocol for conducting such evaluations. The development of such protocol would benefit the community but is out of the scope or this report.

F Vermeer distillation: qualitative results

Figure 14 presents additional qualitative results produced using the Vermeer model and its distilled version.

The images were produced with the following list of prompts.

1. "Ruined circular stone tower on a cliff next to the ocean. Shepherd and sheep on green hillock. Sunrise, big puffy clouds. Naturalistic landscape. Romanticism. Hudson River School. Oil on canvas by Thomas Cole."
2. "Photo of a cute raccoon lizard at sunset, 35mm"
3. "Wallpaper of minimal origami corgi made of multi colored paper, abstract, clean, minimalist, 4K, 8K, soft colors, high definition."
4. "A cat lying a top on the desk on a laptop."
5. "A green stop sign on a pole."
6. "A grey motorcycle on dirt road next to a building."
7. "'Fall is here' written in autumn leaves floating on a lake."
8. "A cake topped with whole bulbs of garlic"
9. "A red plate topped with broccoli, meat and veggies."
10. "A photorealistic image of a chameleon blending seamlessly with its surroundings."
11. "A cat wearing a cowboy hat and sunglasses and standing in front of a rusty old white spaceship at sunrise. Pixar cute. Detailed anime illustration."
12. "A pizza with cherry toppings"

Perfect agreement
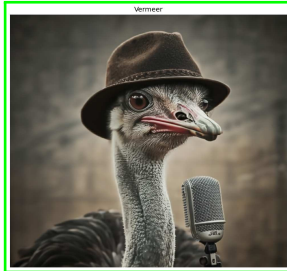
Parti: "a photograph of an ostrich wearing a fedora and singing soulfully into a microphone"
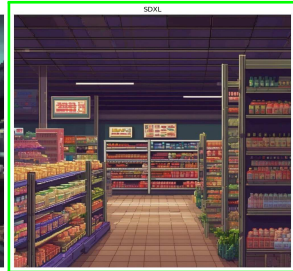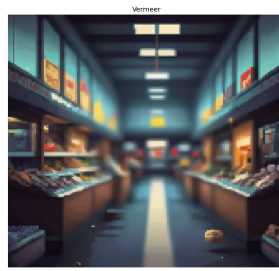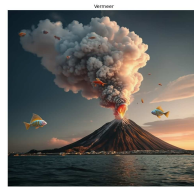
Parti: "pixel art scene, a quiet and empty supermarket at night, atmospheric, 16-bit"
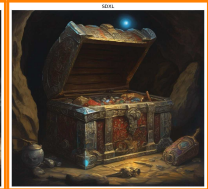
Strong agreement

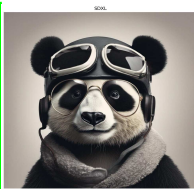

Tifa: "a wood treehouse in an oak tree"
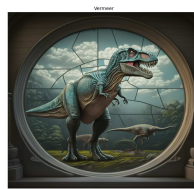
Parti: "a volcano spewing fish into the sky"

Parti: "a painting of an ornate treasure chest with a broad sword propped up against it, glowing in a dark cave"
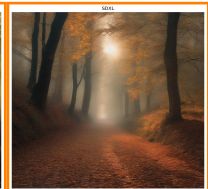
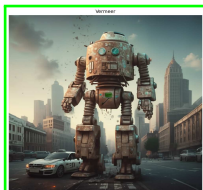Majority agreement

Tifa: "a panda bear with aviator glasses on its head

Tifa: "a stained glass window depicting a calm tyrannosaurus rex"

Parti: "misty autumn forest path, fallen leaves carpeting the ground, sunlight filtering through the trees at daybreak"

Weak agreement

Parti: "a massive robot with a coffee cup head. it is standing in the street with one foot smashing a car."

Parti: "a propaganda poster depicting a cat dressed as french emperor napoleon holding a piece of cheese"

Tifa: "a rusty fire hydrant surrounded by dirt"

Figure 12: Human evaluation pairs, aesthetics preference qualitative results: Vermeer (left), SDXL (right). Green boxes indicate preference cases. Neutral preferences are indicated in orange. Agreement levels indicate the fraction of the 13 evaluators associated with the winning class among three options: "Vermeer is preferred", "SDXL is preferred", and the class indicating neutral preference: "Unsure". Perfect agreement: 100%, Strong agreement: $92 - 77\%$, Majority agreement: $70 - 54\%$, "Weak agreement": $47 - 38\%$. No image has perfect agreement on the neutral preference as neutral.
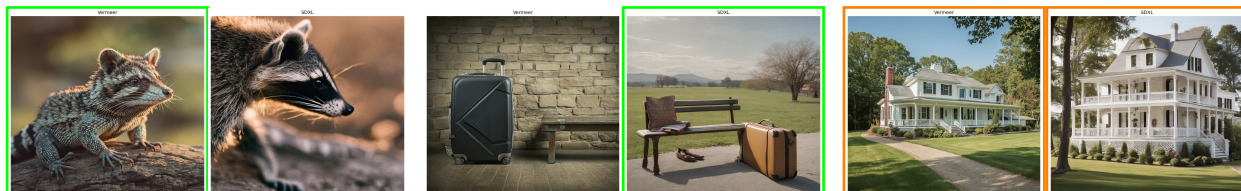
Perfect agreement

Parti: "a photo of the back of a covered wagon. a polar bear is sticking it's head out of the wagon."

Parti: "a photograph of a bird wearing headphones and speaking into a microphone in a recording studio"
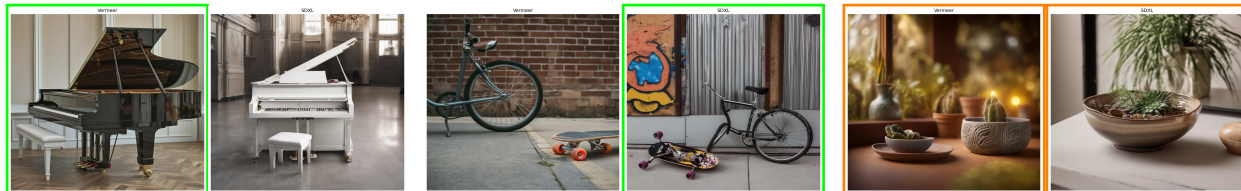
Strong agreement

Parti: "photo of a cute raccoon lizard at sunset, 35mm"

Tifa: "a photo of suitcase and bench; bench is left to suitcase"

Tifa: "a white country home with a wrap-around porch"

Majority agreement

Tifa: "a grand piano with a white bench"

Tifa: "a photo of bike and skateboard; skateboard is left to bike"

Parti: "commercial photography, a hand-crafted ceramic bowl, earth tones, soft lighting, plants"

Weak agreement

Parti: "a white robot with a red mohawk painted as graffiti on a red brick wall."

Tifa: "a photo of dog and stop sign; stop sign is left to dog"

Tifa: "two laptops a mouse cords wires and a monitor"

Figure 13: Human evaluation pairs, consistency preference qualitative results: Vermeer (left), SDXL (right). Green boxes indicate preference cases. Neutral preferences are indicated in orange. Agreement levels indicate the fraction of the 13 evaluators associated with the winning class among three options: "Vermeer is preferred", "SDXL is preferred", and the class indicating neutral preference: "Unsure". Perfect agreement: 100%, Strong agreement: $92-77\%$, Majority agreement: $70-54\%$, "Weak agreement": $47-38\%$. No image has perfect agreement on the neutral preference as neutral.
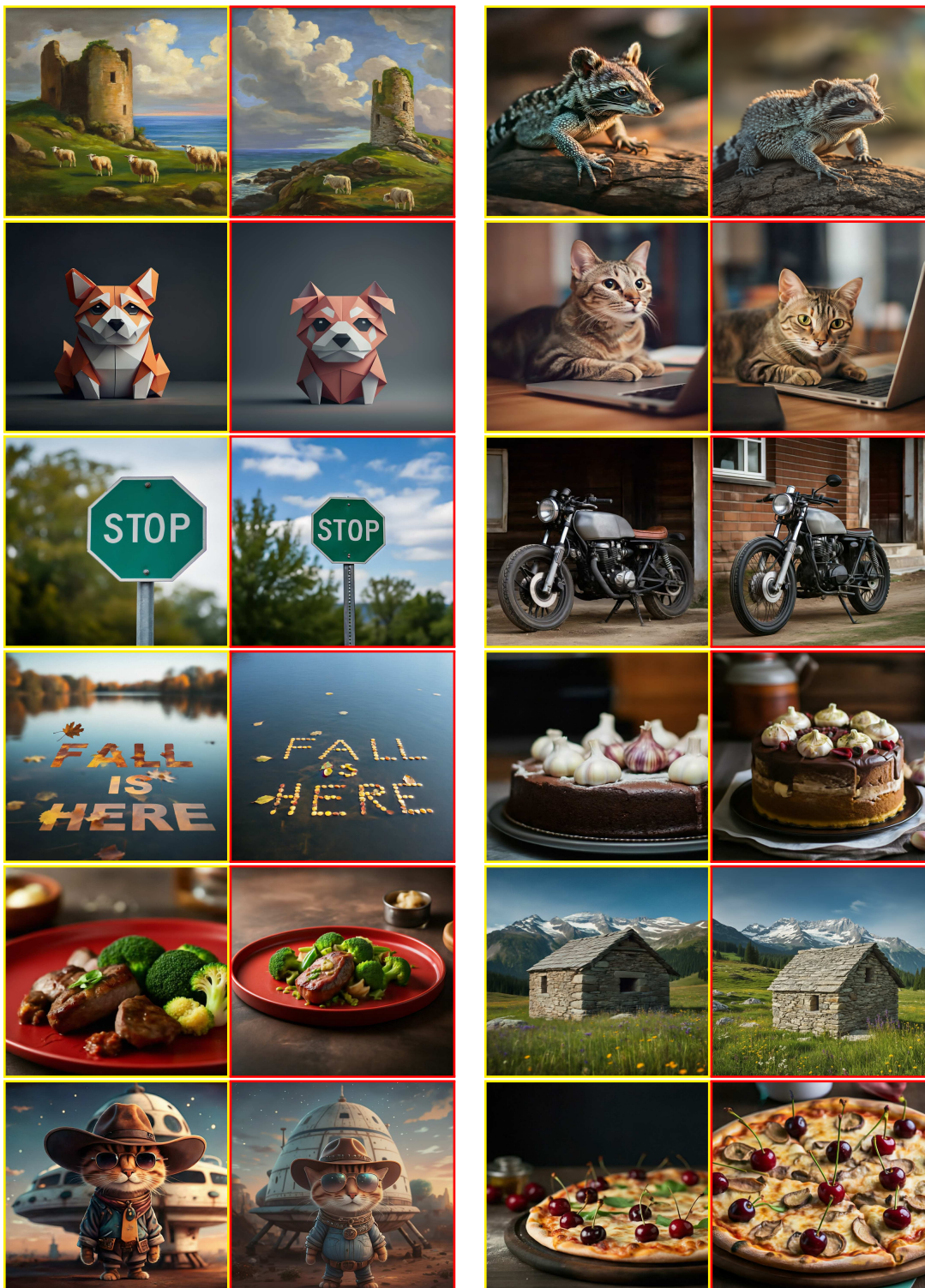
Figure 14: Qualitative comparison between style-tuned Vermeer using 256 steps (red bounding boxes) and its distilled MCM version using 16 steps (yellow bounding boxes). All images are directly generated at 1024x1024 pixels.